Comparison of Sounding, Profiler, Radar and Deilometer Data from Porto Santo Island during ASTEX

by
Eric L. Stevens

Department of Atmospheric Science
Colorado State University
Fort Collins, Colorado

Colorado State University

Department of Atmospheric Science

Paper No. 551

COMPARISON OF SOUNDING, PROFILER, RADAR AND CEILOMETER DATA FROM PORTO SANTO ISLAND DURING ASTEX

by

Eric L. Stevens

Department of Atmospheric Science
Colorado State University
Fort Collins, CO 80523

Spring 1994

Atmospheric Science Paper No. 551

ABSTRACT

COMPARISON OF SOUNDING, PROFILER, RADAR, AND CEILOMETER DATA FROM PORTO SANTO ISLAND DURING ASTEX

Four instruments, the AIR Intellisonde Rawin System, Colorado State University's wind profiling radar, the Wave Propagation Laboratory's 8.7 mm wavelength Doppler cloud radar, and the Belfort laser ceilometer, are described. The data gathered by these instruments at Porto Santo Island during the Atlantic Stratocumulus Transition Experiment (ASTEX), June 1–28, 1992, are also described, and the cleaning of the data is narrated.

Comparisons are then made where more than one instrument measures the same quantity. Radiosonde and wind profiler measurements of wind are split into profiles of wind speed and wind direction and are compared. This comparison reveals that the instruments agree well on both the speed and direction of even subtle features in the wind profile, especially at lower elevations where the profiler is more accurate. Measurements of cloud base height made by the ceilometer, Doppler cloud radar, and radiosonde system are compared, as are the Doppler cloud radar and radiosonde system's measurements of cloud top height. The ceilometer and cloud radar are found to agree well regarding cloud base height when clouds are stratified, even under multiple cloud layers. This agreement fades when the boundary layer becomes less orderly, however. The radiosonde system consistently places cloud layers at slightly lower elevations than the other two instruments do.

Wind direction data below 850 mb are categorized and are found to occasionally deviate from their customary northerly direction. Several characteristics from the cloud

data are also categorized: the number of cloud decks, the degree of stratification of these decks, and the distribution of saturated layers within the radiosonde thermodynamic data. The most common number of cloud decks is found to be two, and these decks typically display moderate stratification. The radiosonde profiles are most frequently completely dry, although the dry profiles alone are not the majority.

ACKNOWLEDGEMENTS

I wish to thank Dr. Wayne H. Schubert for all his help and guidance. If I had any strings to pull back in the old country, I'd see that he received the 1994 Noble Prize for Patience. Thanks must also go to Drs. Jerry Taylor and Michael Montgomery for serving on my committee. Paul Ciesielski and Rick Taft have earned my thanks a hundred times for all their computing assistance. Thanks also to Dr. Richard Johnson for the use of his color printer which was essential to producing understandable cloud deck figures.

This research was supported by the Marine Meteorology Program of the Office of Naval Research under contract N00014-91-J-1422.

CONTENTS

LIST OF FIGURES

LIST OF TABLES

Chapter 1

INTRODUCTION

Several instruments collected data during the Atlantic Stratocumulus Transition Experiment (ASTEX) conducted in the Azores and Madeira Islands region of the north Atlantic from June 1 through 28, 1992. The primary goal of ASTEX was to study the formation, maintenance, and dissipation of marine stratocumulus clouds. While the ASTEX research area covered a large triangular area of the Atlantic (see Figure 1.1), the present paper focuses on data collected by a handful of instruments located on the northern edge of Porto Santo Island (see Figure 1.2). During the summer the Azores High lies to the west of Porto Santo, and northerly winds blow across the island almost continually. The observation site was placed on the northern side of Porto Santo to take advantage of this northerly flow, which helped minimize the effect of the island and preserve the sampled atmosphere's maritime characteristics. Figure 1.3 is a detailed depiction of the observation site.

Colorado State University and the Wave Propagation Laboratory of the National Oceanic and Atmospheric Administration's Environmental Research Lab (NOAA/ERL/WPL) supplied instrumentation to the Porto Santo observation site. CSU provided a surface meteorological station, a five-directional wind profiler which included a Radio Acoustic Sounding System (RASS), a laser ceilometer, a radiosonde system, and an infra-red spectrometer. NOAA/ERL/WPL provided a millimeter wavelength Doppler cloud radar, a microwave radiometer, and a lidar. This paper discusses data gathered by the radiosonde system, the wind profiler, the Doppler cloud radar, and the laser ceilometer.

An outline of this paper is as follows. Chapter Two contains descriptions of the four instruments mentioned above and their data gathered during ASTEX. Data comparisons

are contained in Chapter Three: radiosonde and wind profiler profiles of wind speed and wind direction are compared; ceilometer, Doppler cloud radar, and radiosonde determinations of cloud base are compared; and Doppler cloud radar and radiosonde determinations of cloud top are compared. Also included in Chapter Three are several categorizations of the wind and cloud data. Averaged wind direction below 850 mb is classified, as are the number of cloud decks, the degree of saturation within these cloud decks, and the distribution of saturated layers within the radiosonde thermodynamic data. Finally, a brief summary and conclusions are presented in Chapter Four.

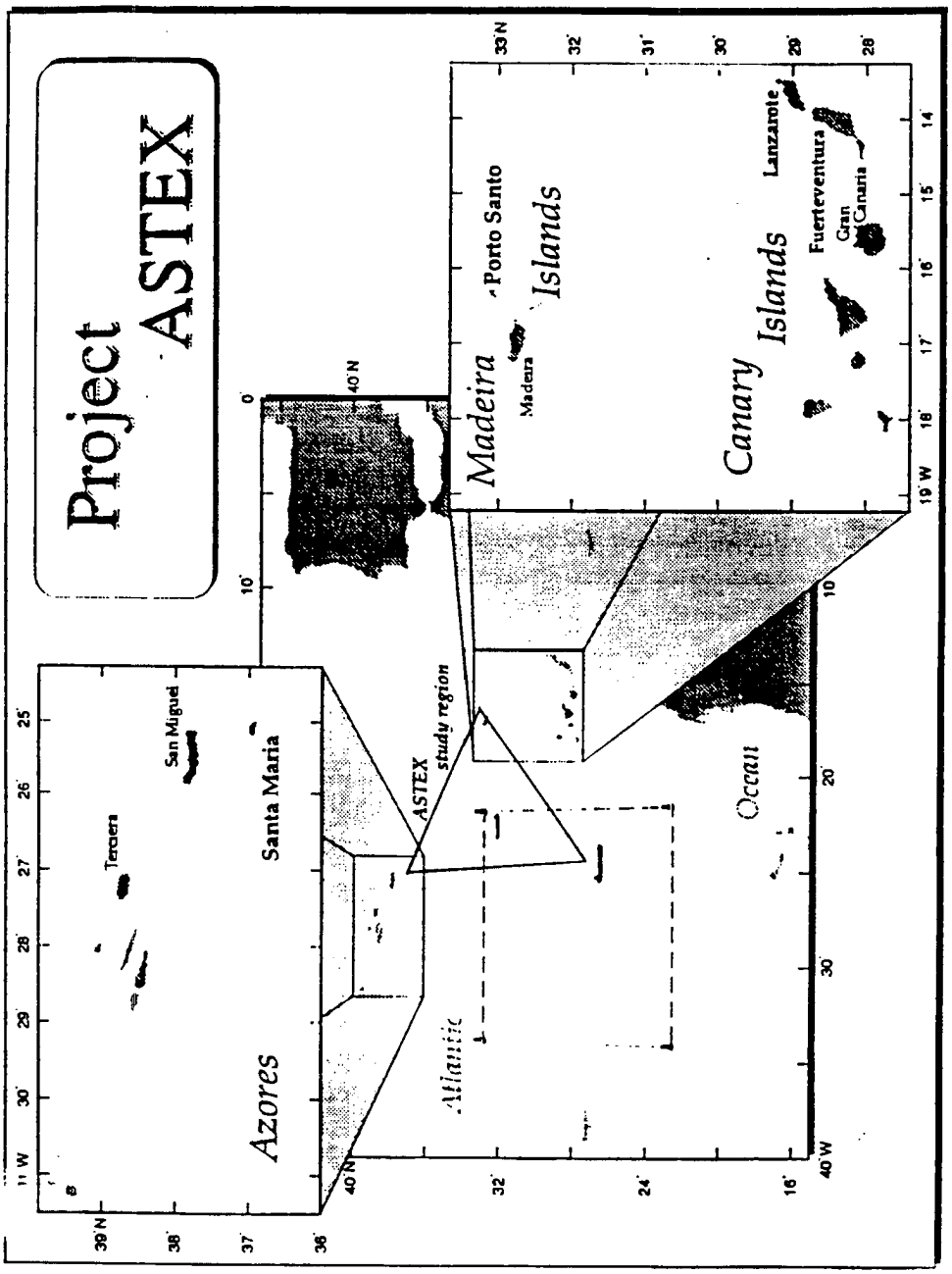

Figure 1.1: Map of the ASTEX region showing the triangular array of wind profiler/upper air measurements and the array of buoys associated with the oceanographic subduction experiment. From ASTEX Operations Plan, page 24.

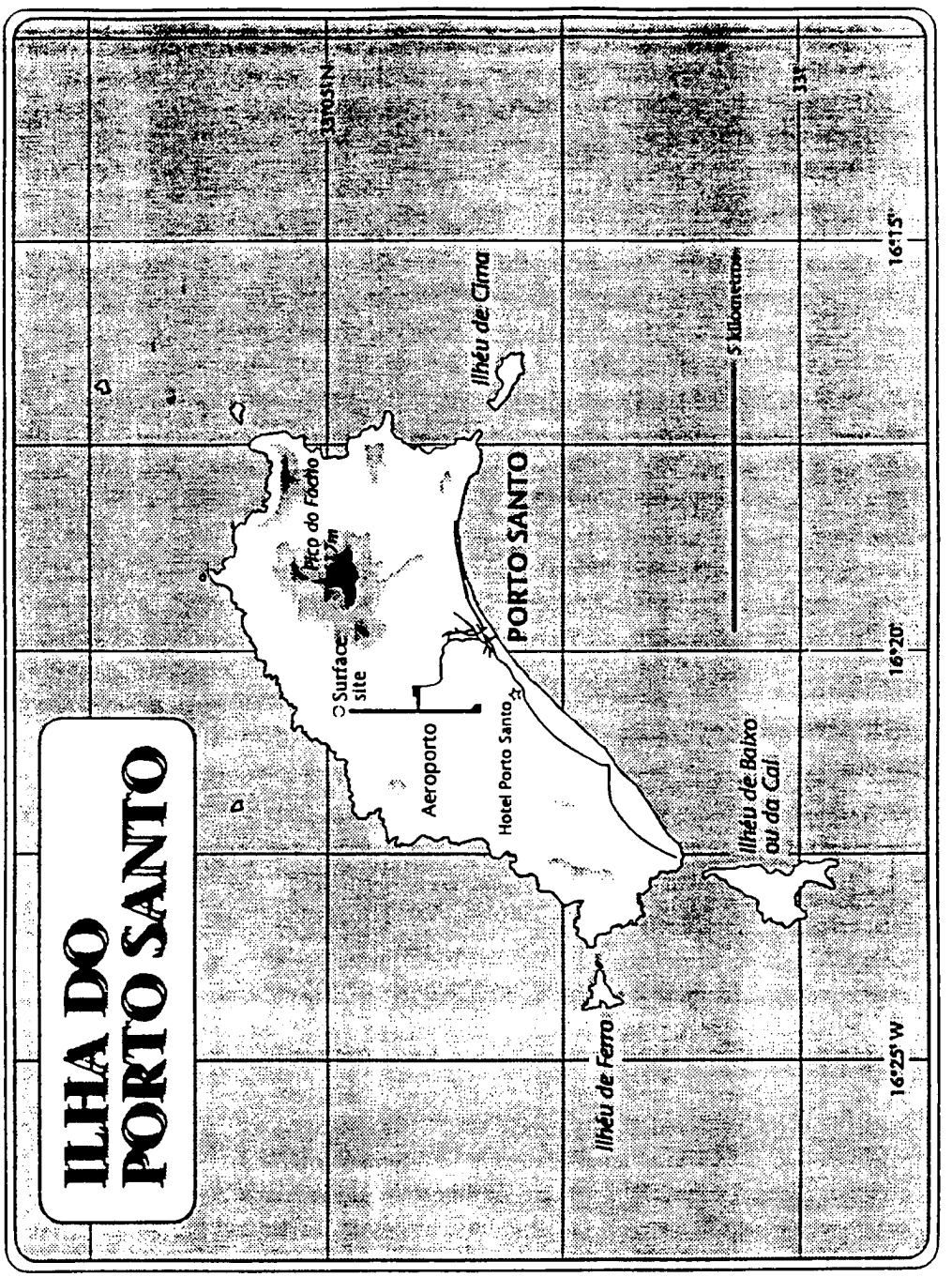

Figure 1.2: Map of Porto Santo Island. The observation site, labeled here as Surface Site, was centered at coordinates 33°5′2″ N latitude and 16°20′49″ W longitude, stood at an elevation of 97m above sea level, and was located 295m north of the airport runway. From ASTEX Operations Plan, page 61.

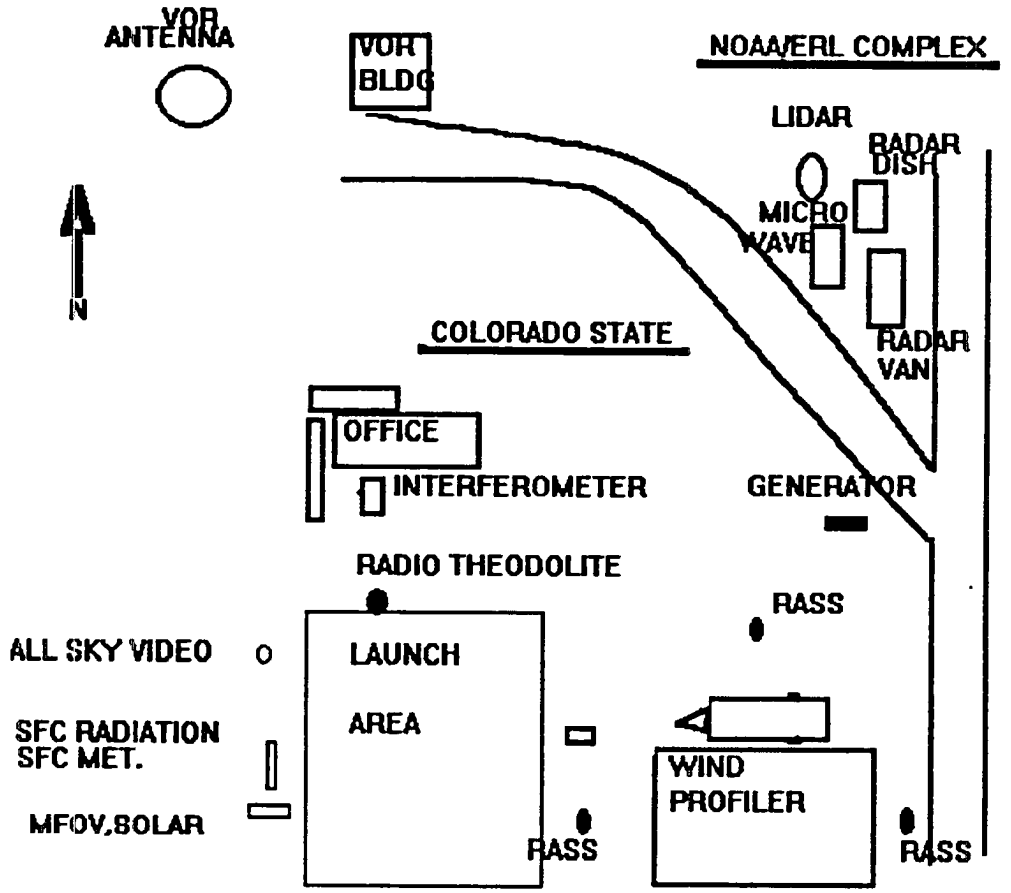

Figure 1.3: The Porto Santo observation site and its instruments. For the purposes of this paper, we are concerned with Colorado State's radiosonde system, which included the radio theodolite and the region marked "Launch Area," the wind profiler including RASS stations, and the laser ceilometer. as well as NOAA/ERL's radar. From Cox et al. (1993).

Chapter 2

THE INSTRUMENTS

While many instruments gathered data during ASTEX at a number of different locations, this paper is concerned with the radiosonde system, wind profiling radar, Doppler cloud radar, and laser ceilometer, all located at the observation site shown in Figure 1.2. This chapter outlines the functions of these four instruments and describes the data generated by each.

2.1 Radiosonde System

A radiosonde, or sonde, consists of a foam box containing instruments which measure the temperature, relative humidity, and pressure of the surrounding air. Other pieces of the system include a balloon, a radio theodolite, which receives the sonde's data transmissions and tracks the location of the sonde as it ascends, and a small computer, which stores the sonde's data and uses these data to derive other quantities besides temperature, relative humidity, and pressure. The sonde is readied and its instruments are calibrated during a preflight stage, after which the sonde is carried aloft by a balloon. The ascending sonde continually transmits temperature, relative humidity, and pressure data back to the ground station until the balloon bursts at an elevation as high as 30km. The sonde's entire journey, from preflight stage to maximum altitude, can last as long as two hours.

Since there are small variations in performance between the temperature, relative humidity, and pressure instruments from sonde to sonde, each of these instrument's individual calibration values must be entered into the ground station computer so that the computer may properly interpret the sonde's data. The sonde's instruments are calibrated when they are produced, and the proper calibration information is included with

each sonde. These calibration values are simply entered into the computer during the preflight stage. The radiosonde's batteries, which provide power for transmitting data to the surface, are also connected during this preflight stage. Depending on the model of sonde used, the batteries could be dry or wet cell. Wet cell batteries, which must be soaked in water for a time before being inserted into the sonde, are occasionally preferred because of their good performance in the cold environment encountered at higher altitudes. Once the batteries are connected, the sonde begins transmitting data, and the radio theodolite is locked onto the sonde's location even though the sonde has not yet been launched. If the transmitted signal is too weak, or if the data appear faulty, the sonde is rejected and a different sonde is used. If no problems appear, the sonde is attached to a helium or hydrogen-filled balloon and released.

As the balloon ascends, the sonde continuously samples the air temperature, relative humidity, and pressure, and transmits these data to the ground station. At the ground, the radio theodolite locks onto this transmission to continually track the location of the ascending sonde. The radio theodolite records the sonde's angle of elevation from the horizon as well as the sonde's azimuth, which is the horizontal angle between true north and the point on the ground directly under the sonde. Thus, raw radiosonde data consists of temperature, relative humidity, pressure, and azimuth and elevation angles as functions of time. These data are all stored in the ground station computer.

2.1.1 The ASTEX radiosonde system

The radiosondes used during ASTEX were Intellisonde model IS-4A-1680 radiosondes, manufactured by Atmospheric Instrumentation Research (AIR) Incorporated, Boulder, Colorado. An AIR sonde (pictured in figure 2.1) measured 10cm square at the base, 15cm high, and had a mass of 240g. The sonde measured pressure with an aneroid sensor whose capacitance varied with pressure. The transfer function which translated capacitance to pressure was a fifth-order polynomial whose coefficients were different for each sonde. These calibration coefficients were stored in the sonde and transmitted to the radiotheodolite during the preflight stage. Temperature and relative humidity were measured with resistive sensors, both Manufactured by VIZ. The temperature sensor was

a rod thermistor whose lock-in value was printed on the radiosonde body and was entered into the computer during the preflight phase. Relative humidity was measured with a VIZ Accu-Loc humidity sensor, a variety of carbon strip hygristor. These sensors were both individually calibrated at 25°C and 33% relative humidity. The relative humidity sensor was removed from its foil package and its lock-in value was also entered into the computer before launch. The humidity sensor, or hygristor, was inserted into a sun-shielded compartment in the upper third of the sonde. As the sonde rose, air entered the hygristor compartment through the top of the sonde, flowed past the hygristor, and exited through the side of the sonde. The helium-filled balloons (some sondes released early in the experiment were inflated with hydrogen, due to a helium shortage) ascended at approximately 4-5 ms^{-1}, a rise rate providing adequate flow past the hygristor. The bottom of each sonde was a ground plate out of which extended a quarter-wave antenna which transmitted data to the surface at a frequency of 1680MHz. The AIR sonde's power was supplied by two nine-volt alkaline (dry cell) batteries.

The entire AIR system used during ASTEX was the Intellisonde Rawin System (Model IS-4A1-MET). In addition to the sondes, this system included an automatically tracking radio theodolite (shown in figure 2.2), a PC-AT compatible computer with an AIR Metdecoder board in one of its expansion slots, and a supply of 200g balloons. The computer had an auto-launch feature which automatically began recording data once a 0.8mb drop in pressure was detected.

2.1.2 Analysis of thermodynamic data

Instrument time lag

As a sonde ascends through the atmosphere, it encounters changes in the temperature of the surrounding air, and the sonde's temperature sensor experiences a time lag; that is, the sensor requires a certain amount of time to notice a temperature change, and thus errors are generated in the sonde's data.

Let T denote the sensor temperature and T_e denote the environmental temperature. According to the Newtonian cooling law, T and T_e are related by the first order differential

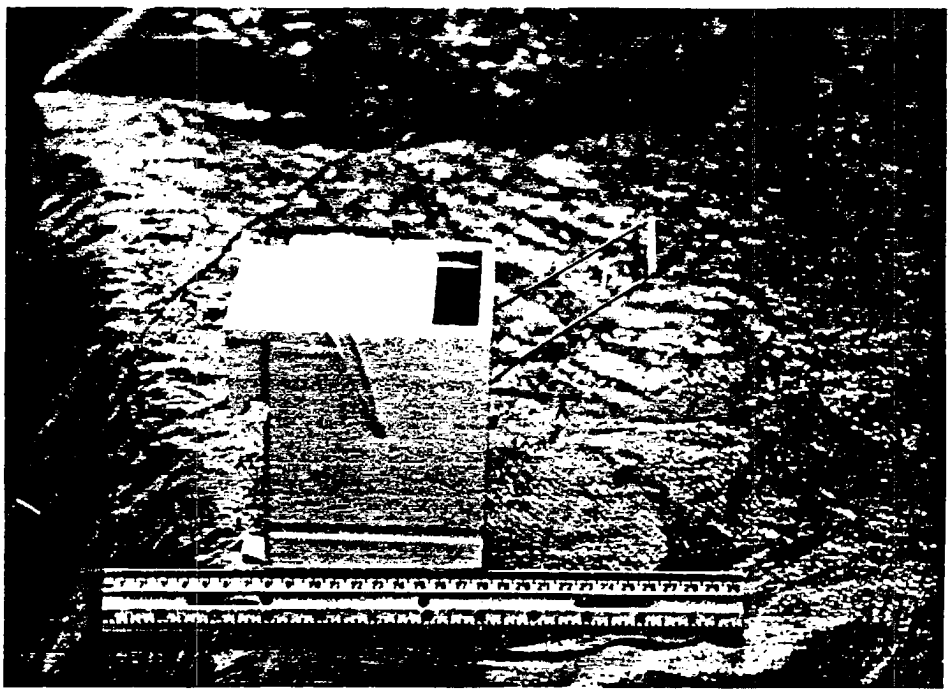

Figure 2.1: An AIR Intellisonde. The rod thermistor extends from the right side of the sonde. The hygristor lies within the radiation-shielded compartment at the top of the sonde. As the sonde assends, air enters the compartment through the inlet at the top of the sonde and then flows horizontally across the hygristor before exiting downward at the left side of the sonde. The sonde transmits via a quarter wave antenna extending from the sonde's bottom (not visible in this figure). From Schubert (1992).

Figure 2.2: John Kleist (left) and William Cotton prepare to launch a sonde under windy, stratocumulus conditions on Porto Santo. Between them is the automatically tracking radiotheodolite, which measures azimuth and elevation angles of the balloon. From Schubert (1992).

equation

$$\frac{dT}{dt} = -\frac{1}{\tau}(T - T_e), \tag{2.1}$$

where τ is the sensor's response time. We will assume that the environmental temperature changes linearly in time as the sonde ascends so that $\frac{dT_e}{dt} = \lambda$. The above equation can then be written

$$\frac{d(T - T_e)}{dt} + \frac{1}{\tau}(T - T_e) = -\lambda, \tag{2.2}$$

which has the initial value problem solution

$$T - T_e = [(T - T_e)_0 + \lambda\tau]e^{-\frac{t}{\tau}} - \lambda\tau, \tag{2.3}$$

If enough time passes for the initial condition $(T - T_e)_0$ to be forgotten, the sensor temperature and the environmental temperature will differ by $-\lambda\tau$, or

$$T - T_e = -\lambda\tau. \tag{2.4}$$

If the balloon is carrying the sonde aloft at a rate of 5ms^{-1} through an atmosphere with a dry adiabatic lapse rate (a cooling with height of roughly 10°C per km), then λ = -0.05Ks^{-1}. The lag of the temperature sensor is between 3 to 5s, yielding $-\lambda\tau \approx 0.2$K, that is, a temperature sensor in this environment reads approximately 0.2K too warm. However, if the sonde were rising through a temperature inversion in which the air warmed 5K through a 100m layer, then $\lambda = 0.25\text{Ks}^{-1}$, and $\lambda\tau \approx 1.0$K, which means the temperature sensor would read approximately 1.0K too cold.

The AIR sonde's humidity sensor also experiences a time lag. Unlike the temperature sensor whose time lag is uniformly between 3 and 5s, the lag of the humidity sensor depends on temperature. At 25°C, the lag constant τ is between 1 and 2s, at 0°C it is between 3 and 5s, and below -20°C it is between 5 and 10s. If we use equations similar to those above but derived specifically for the humidity sensor and take into account the slow rate of increase of relative humidity in the boundary layer and the 2s lag of the temperature sensor, the relative humidity sensor reads too dry by a few tenths of a per cent. The region just above cloud top is a local area of significant change, however, and a 60% decrease in humidity

through a 100m layer above cloud top yields a relative humidity reading approximately 6% too high.

These lag effects in temperature and relative humidity data are not always negligible, especially in strong inversions, but no attempt was made to correct these errors in the ASTEX radiosonde data.

Initial data cleaning

Raw radiosonde data collected at ASTEX consisted of pressure, temperature, and relative humidity data, as well as azimuth and elevation angles, all recorded as functions of time. The AIR software stored these data in files along with several derived quantities generated from the raw data by the AIR software itself. Table 2.1 presents a sample of raw radiosonde data and its AIR-generated derivatives. These data files were referred to as "Level I" data.

From these Level I data, a Level II data set was produced. On the way from Level I to Level II, interpolation was neccessary to obtain a data set equally spaced in time or height; the data set shown in table 2.1 is not evenly spaced. Additionally, although the average rate of pressure change is around -0.5 mb per second (about a $5ms^{-1}$ ascent rate), there are irregularities in the data of pressure versus time. Occasionally the same pressure reading was even found at different altitudes. Stratocumulus clouds are not known for vertical winds strong enough to force balloons downward, and thus the nonmonotonic nature of the pressure profiles was probably due to deficiencies is the sondes' pressure sensors. Pressure data that were obviously bad were deleted, and a smoothing of the resulting pressure profiles was performed.

The Level II thermodynamic data were produced from the Level I data in the following manner. First, a number of data points were eliminated. Often a sonde continued transmitting data even after its balloon had burst and the sonde was rapidly falling back to earth. Occasionally the balloon failed to burst but instead developed a slow leak and hovered at an elevation for a time before eventually sinking. All such non-ascending data were eliminated, and in general, any data that appeared obviously bad for any reason were deleted. Next, a cubic spline interpolation function was fit to the raw data pairs of time

TIME	PMB	TEMP	TDEW	RH%	GEOPM	AZDEG	ELDEG	SPEED	DIR	E.TIME
05:02:41.93	1009.10	17.40	14.65	84.00	97	159.93	5.63	1.5	355	0.00
05:02:43.09	1006.96	17.41	15.43	88.26	115	157.30	16.70	1.5	355	1.16
05:02:46.49	1004.29	17.24	15.24	88.11	138	146.82	27.67	4.3	312	6.87
05:02:48.80	1002.91	17.13	15.12	88.03	150	149.32	30.15	4.7	313	9.18
05:02:51.16	1001.72	17.02	15.01	88.05	160	145.77	32.67	5.0	312	11.54
05:02:53.47	1000.66	16.92	14.93	88.14	169	146.27	34.67	5.2	313	13.85
05:02:55.83	999.26	16.82	14.88	88.40	181	143.60	35.60	5.5	313	16.21
05:02:58.14	997.77	16.71	14.79	88.54	194	142.90	37.53	5.3	312	18.52
05:03:00.50	996.44	16.61	14.74	88.85	205	141.70	37.53	5.2	312	20.88
05:03:02.86	995.12	16.49	14.70	89.22	216	140.02	38.58	5.1	312	23.24
05:03:05.22	993.80	16.38	14.58	89.18	228	139.38	38.58	5.1	312	25.60
05:03:07.58	992.36	16.27	14.48	89.22	240	137.52	39.58	4.7	307	27.96
05:03:09.95	990.93	16.15	14.38	89.35	252	137.10	40.35	4.5	305	30.33
05:03:14.72	988.34	15.93	14.28	89.99	275	135.43	41.03	4.9	305	35.10
05:03:17.09	986.78	15.82	14.25	90.49	288	134.68	41.05	4.7	304	37.47
05:03:19.50	985.72	15.71	14.29	91.34	297	134.00	41.88	4.7	304	39.88
05:03:21.97	984.34	15.61	14.36	92.35	309	134.13	42.22	4.6	304	42.35
05:03:24.45	983.20	15.50	14.35	92.98	319	132.88	41.88	4.5	303	44.83
05:03:26.92	981.77	15.40	14.37	93.68	331	132.43	41.75	4.6	304	47.30
05:03:29.39	980.49	15.29	14.43	94.71	342	132.70	42.13	4.5	305	49.77
05:03:31.92	979.28	15.19	14.40	95.16	353	133.63	41.72	4.5	305	52.30
05:03:36.97	976.59	14.98	14.48	96.94	376	133.15	41.88	4.8	308	57.35
05:03:39.55	975.58	14.88	14.51	97.76	385	133.38	42.22	4.8	310	59.93
05:03:42.13	974.23	14.78	14.52	98.46	397	133.57	42.38	4.7	310	62.51
05:03:44.71	972.89	14.66	14.44	98.67	408	132.85	42.47	4.9	313	65.09
05:03:47.35	971.67	14.57	14.39	98.96	419	132.98	42.28	4.9	314	67.73
05:03:49.93	970.33	14.46	14.32	99.21	431	132.85	42.35	5.0	313	70.31
05:03:52.57	969.24	14.35	14.23	99.33	440	132.60	42.33	4.9	314	72.95
05:03:55.20	967.92	14.25	14.15	99.41	452	131.88	42.22	5.1	314	75.58
05:03:57.79	966.57	14.15	14.08	99.64	464	132.23	42.25	4.9	314	78.17
05:04:00.42	965.24	14.06	14.01	99.79	475	132.20	42.13	5.0	313	80.80
05:04:03.11	963.85	13.97	13.94	99.88	488	131.90	41.95	5.2	315	83.49
05:04:03.11	962.46	13.87	13.84	99.91	500	132.38	42.00	5.3	315	83.49
05:04:06.68	961.15	13.80	13.77	99.94	511	132.57	41.95	5.2	315	87.06
05:04:10.25	959.82	13.74	13.72	99.96	523	132.93	41.88	5.3	318	90.63
05:04:13.49	958.42	13.66	13.64	100.00	535	133.35	42.00	5.6	320	93.87
05:04:16.30	957.09	13.58	13.56	100.00	547	133.52	41.67	5.6	322	96.68
05:04:18.99	955.63	13.47	13.45	100.00	560	133.88	41.78	5.8	323	99.37
05:04:21.62	954.60	13.40	13.38	100.00	569	134.07	41.50	5.7	325	102.00
05:04:24.26	953.23	13.35	13.33	100.00	581	134.30	41.05	5.5	327	104.64
05:04:26.90	952.00	13.27	13.26	100.00	592	134.60	41.13	5.7	328	107.28
05:04:29.59	950.71	13.21	13.19	100.00	603	134.80	40.95	5.7	328	109.97
05:04:32.22	949.27	13.12	13.10	100.00	616	135.38	40.97	6.0	328	112.60

Table 2.1: Sample of Level I radiosonde data, taken from the 0548 GMT launch on June 6, 1992. The data columns from left to right are: TIME=time of day using Porto Santo local time; PMB=pressure in mb; TEMP=temperature in °C; TDEW=dew point temperature in °C; RH%=per cent relative humidity; GEOPM=geopotential height above sea level in feet; AZDEG=azimuth angle from true north; ELDEG=angle of elevation above the horizon; SPEED=horizontal wind speed in ms^{-1}; DIR=direction wind is blowing from in degrees clockwise from from true north; E.TIME=time elapsed since the balloon's release.

and pressure (t_i, p_i) where $i = 1, 2, 3, ...$ to obtain a continuous function $p(t)$. Since noise in the pressure sensor occasionally caused $p(t)$ to be nonmonotonic, $p(t)$ was sampled at intervals of three seconds, and then an eleven point filter was applied. This filter had the weights (-1,-5,-5,20,70,98,70,20,-5,-5,-1)/256 and had the spectral response shown in figure 2.3. The net effect of this filter was to remove oscillations having periods shorter than 18 seconds. A detailed description of this filer can be found in Hamming (1983, pages 143-144). Next, a cubic spline was fit to the pressure data, thus obtaining the monotonic continuous function $\bar{p}(t)$, which was then evaluated at the original t_i to produce $\bar{p}_i$. Filtered pressure data were then converted into height data using the discrete hydrostatic relation

$$z_i = z_{i-1} + \frac{R}{2g}(T(t_i) + T(t_{i-1})) \ln\left(\frac{\bar{p}(t_{i-1})}{\bar{p}(t_i)}\right). \tag{2.5}$$

This upward integration commenced at the 97m launch elevation. A cubic spline was then fit to the (z_i, t_i) data to obtain the continuous function $t(z)$. From the continuous function $t(z)$, t_j were found corresponding to equally spaced 10m intervals in z_j. Temperature and relative humidity were then linearly interpolated from the nearest two times to obtain data at equally spaced intervals in height. Finally, from the temperature T and relative humidity U data, dew point temperature T_d was derived. Saturation vapor pressure $e_s(T)$ was computed from

$$e_s(T) = 6.112 \exp\left(\frac{17.67(T - 273.15)}{T - 29.65}\right) \tag{2.6}$$

where $e_s(T)$ is in millibars and T is in Kelvin. Actual water vapor pressure e is computed from

$$e = U e_s(T). \tag{2.7}$$

Equation (2.6) is Bolton's (1980) fit to the highly acurate (0.005%) formula of Wexler (1976). The accuracy of (2.6) is 0.1%. Since dew point temperature T_d is defined by $e_s(T_d) = e$, (2.6) can be rearranged to obtain

$$T_d = 273.15 + \frac{243.5 \ln(\frac{e}{6.112})}{17.67 - \ln(\frac{e}{6.112})}, \tag{2.8}$$

which allows calculation of T_d from vapor pressure e.

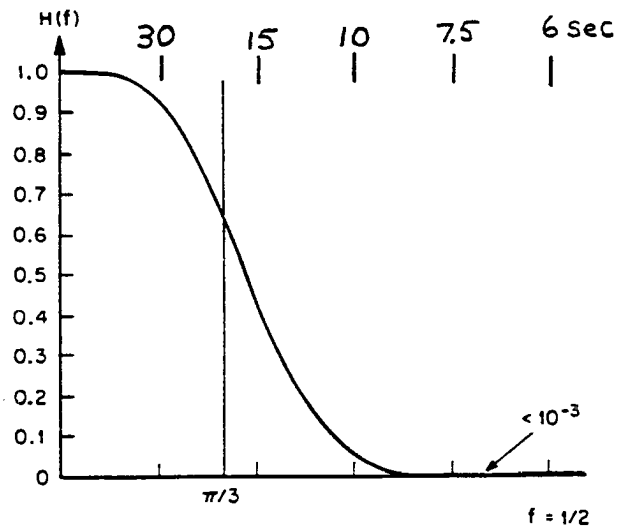

Figure 2.3: Monotone spectral response of the filter used in processing radiosonde thermodynamic and wind data. The lower abscissa is labeled in frequency (where $f = 1/2$ corresponds to one-half oscillation per data point), and the upper abscissa is labeled in period (seconds) assuming a three second interval between data points. This filter effectively removes all oscillations with periods shorter than 18 seconds. From Schubert (1992).

2.1.3 Analysis of the wind data

When calculating a wind profile from radiosonde data, it is assumed that any horizontal movement of the sonde is due the sonde being advected, or pushed, by the wind. This assumption is not completely correct, however. A sonde is carried aloft by its balloon through a vertically sheared wind field, and the balloon requires some time to accelerate or decelerate to match the velocity of the surrounding air in each layer. Thus a sonde experiences a time lag in its wind data much like the lag experienced in its temperature and humidity measurements. A second flaw in the assumption that the sonde moves with the airflow is self-induced balloon motion—a tendency for a balloon to snake its way aloft rather than rise straight up. These issues regarding how well balloons follow the air flow are discussed in the following subsections.

Inertial lag of the balloon

A spherical balloon filled with hydrogen or helium has an amount of upward lift

$$L = \rho V g, \tag{2.9}$$

where ρ is the air density, V is the balloon volume, and g is gravitational acceleration. The sum of the balloon, gas, suspension line, and radiosonde has a mass m and experiences a downward gravitational force mg. A rising balloon experiences a downward drag force

$$\frac{1}{2} c_D \rho A w^2 = \text{Drag}, \tag{2.10}$$

where c_D is the drag coefficient, which is typically about 0.4 according to Schubert et al. (1992), A is the cross-sectional area of the balloon, and w is the balloon's rise rate (typically about 5ms^{-1}). This calculation of the drag force neglects any drag contributed by the sonde itself. For a steadily ascending radiosonde the drag and gravitational forces balance the lift force, i.e.,

$$\frac{1}{2} c_D \rho A w^2 + mg = \rho V g. \tag{2.11}$$

Typical values of the drag, gravitational, and lift forces are 8, 5, and 13 Newtons respectively.

If the balloon rises through sheared layers in the airflow, the drag force is not in the vertical direction but rather in a direction opposite to the motion of the balloon relative to the moving air. The horizontal component of this drag force will accelerate or decelerate the balloon until the balloon's velocity matches that of the air. The formal solution of this problem has been given by Perkins (1952), who concludes that the measured wind is a weighted average of the actual wind over a layer whose thickness is

$$d = \frac{6m}{c_D \rho A}. \tag{2.12}$$

Retaining (2.11) as the approximate force balance in the vertical, $c_D \rho A$ can be eliminated between (2.11) and (2.12) to obtain

$$d = \frac{3w^2}{g(\gamma - 1)}, \tag{2.13}$$

where $\gamma = \frac{L}{mg}$ is the lift ratio. Note that $\gamma > 1$ is a necessary condition for the balloon to rise. For rise rates $3 < w < 6 \text{ms}^{-1}$ and lift ratios $2 < \gamma < 3$, equation (2.13) yields $1 < d < 11\text{m}$. The sampling interval is approximately 10m, and we can thus assume that lag effects in the wind data are negligible.

Self-induced balloon motions

An ascending spherical balloon has a tendency to snake its way aloft instead of rising along a linear path. McVehil et al. (1965) tracked one-meter and two-meter diameter balloons with a pulsed Doppler radar which yielded high vertical resolution soundings of the radial (along the radar beam) velocity component of the balloon. A two-meter diameter balloon rising at 8 ms^{-1} was found to weave about its vertical path in oscillations with vertical wavelengths from 30 to 80m. One-meter diameter balloons were found to have similar oscillations, but with vertical wavelengths of approximately 15m. McVehil et al. concluded that one-meter and two-meter balloons do not move entirely with the wind, but have additional oscillatory components whose causes are aerodynamic, not meteorological. The wind speed errors associated with these spurious oscillations were expected to be between 1 and 2.5 ms^{-1}.

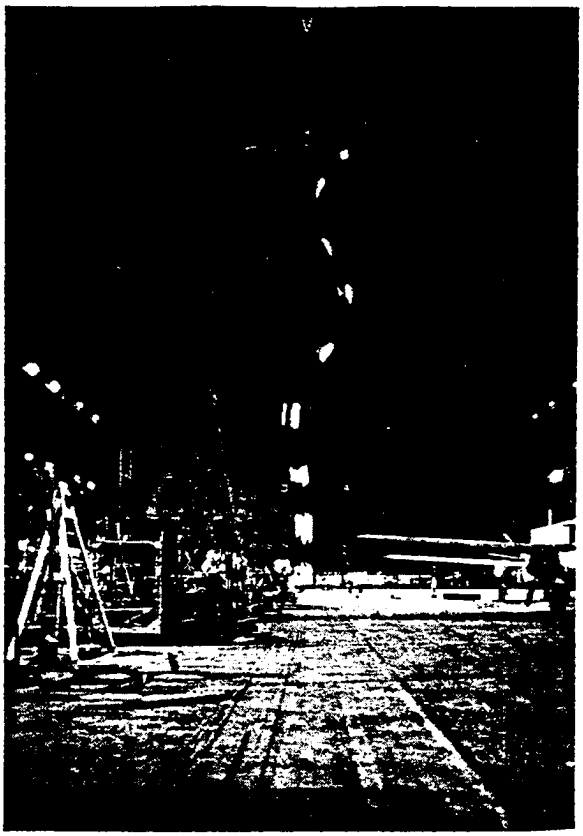

Figure 2.4: Self-induced balloon motion shown by a balloon released in a derigable hangar. A strobe light flashed every $\frac{1}{4}$second to produce this photograph. From Murrow(1965).

Self-induced motions of flexible rubber balloons and rigid mylar balloons were also observed by Murrow and Henry (1965) in a large dirigible hangar at Lakehurst, New Jersey. The hangar's doors and windows were closed and the air inside was allowed to settle. The balloons were then released in the still air and their deviations from a linear vertical ascent were measured with phototheodolites (see figure 1.5). The root-mean-square (rms) horizontal velocity, where rms is the square root of the mean of the squared deviations from the population mean, was proportional to the terminal vertical velocity. Smooth rigid spheres of two-meter diameter had rms horizontal velocities approximately one-half the terminal vertical velocity. Scoggins (1965) found that balloons covered with rough surface protrusions such as small cups or spikes suffered less dramatic self-induced

motion. The flexible rubber balloons used during ASTEX probably produced self-induced motions, although the radiosonde train may have dampened the effect somewhat.

In order to remove the effects of inertial lag (which was just analyzed) and self-induced motion of the balloon, the AIR software filtered the Level I wind data by taking layer averages of the vector wind components u and v. Details of this filtering process have not been released by AIR. Thus there is no way of knowing how AIR coped with self-induced balloon motions, and it may be misleading to examine the wind data at vertical resolutions higher than approximately 100m.

2.1.4 The ASTEX data set

The entire ASTEX data set contains 203 soundings from June 1 through June 28. Generally the balloons were launched every three hours for the duration of the experiment. Consult Schubert et al. (1992) for a complete description of the ASTEX soundings, including profiles of each sounding's thermodynamic data.

2.2 CSU Wind Profiler

Instruments which determine wind fields detect the presence of some tracer in the air, and assume that any horizontal motion of the tracer is due to the tracer's being advected by the ambient flow, and thus the ambient flow is itself deduced. While a radiosonde system determines horizontal winds by tracing the motions of an ascending balloon, wind profiling radars determine the three-dimensional wind field by detecting and tracking eddies in the air itself. A wind profiling radar, or wind profiler, consists of a radar system, which transmits and receives electromagnetic signals, and a processing system, which controls the radar and interprets the collected data.

A wind profiler operates as follows. The profiler's radar system transmits a pulse of electromagnetic radiation and then waits to receive return signals. The transmitted pulse is aimed straight up to the zenith and is confined within a very narrow beam. A return signal is generated when the electromagnetic pulse encounters an eddy in the air flow. Compared to the surrounding air, turbulent eddies contain temperature, pressure, and humidity irregularities. Since the air's index of refraction (the ratio of electromagnetic

	z(m)	p(mb)	t(c)	td(c)	wind speed (m/s)	wind direction (degrees)
1	97.	1009.10	17.40	14.65	1.50	355.00
2	100.	-99.99	-99.99	-99.99	-99.99	-99.99
3	110.	1007.56	17.41	15.42	15.19	291.59
4	120.	1006.39	17.36	15.39	11.43	54.04
5	130.	1005.20	17.31	15.33	7.40	146.44
6	140.	1004.01	17.24	15.26	2.68	254.50
7	150.	1002.83	17.13	15.13	3.73	317.94
8	160.	1001.65	17.01	15.02	3.66	315.00
9	170.	1000.47	16.91	14.94	4.12	312.87
10	180.	999.29	16.83	14.90	4.19	265.48
11	190.	998.11	16.73	14.82	4.52	265.82
12	200.	996.93	16.64	14.78	5.19	272.17
13	210.	995.76	16.55	14.74	4.98	107.04
14	220.	994.58	16.45	14.67	4.68	282.33
15	230.	993.41	16.35	14.57	4.83	17.26
16	240.	992.24	16.26	14.48	4.49	333.22
17	250.	991.07	16.16	14.40	3.93	227.06
18	260.	989.90	16.06	14.35	4.19	278.17
19	270.	988.73	15.97	14.31	4.51	252.70
20	280.	987.56	15.87	14.28	4.47	105.41
21	290.	986.39	15.77	14.28	4.29	72.68
22	300.	985.22	15.68	14.33	4.37	44.21
23	310.	984.06	15.58	14.37	4.66	289.99
24	320.	982.89	15.48	14.37	4.80	299.07
25	330.	981.73	15.39	14.39	4.98	310.20
26	340.	980.57	15.29	14.44	5.32	268.67
27	350.	979.41	15.21	14.42	5.06	281.13
28	360.	978.24	15.11	14.45	4.45	302.11
29	370.	977.09	15.01	14.49	3.75	278.88
30	380.	975.93	14.92	14.52	3.72	283.54
31	390.	974.77	14.82	14.53	4.01	283.81
32	400.	973.62	14.72	14.50	4.29	286.59
33	410.	972.46	14.63	14.44	4.48	290.04
34	420.	971.30	14.54	14.39	4.54	293.14
35	430.	970.15	14.44	14.32	4.63	294.99
36	440.	969.00	14.34	14.23	4.73	299.00
37	450.	967.85	14.24	14.16	4.91	306.05
38	460.	966.70	14.16	14.10	5.36	259.34
39	470.	965.55	14.08	14.04	5.59	274.31
40	480.	964.40	14.02	13.99	5.96	291.69
41	490.	963.25	13.94	13.92	6.06	304.09
42	500.	962.11	13.84	13.83	5.41	304.37

Table 2.2: Sample of Level II radiosonde data from 0548 GMT, June 6, 1992, which corresponds to the data displayed in table 2.1. The data columns from right to left are: z(m)=height of sonde above sea level in meters; P(mb)=pressure in mbs; T(c)=temperature in °C; Td(c)=dew point temperature in °C; SPEED(m/s)=horizontal wind speed in meters per second; DIRECTION(degrees)=direction in degrees from true north that the wind is blowing from. Note that in this paper, the Level II winds seen above are not used—all comparisons between radiosonde winds and wind profiling radar winds are made using Level I radiosonde wind data.

radiation's speed through free space to its speed through the medium in question) depends primarily on temperature, pressure, and humidity, these eddies contain irregularities in this index. When the electromagnetic signal encounters an eddy, the local variations in the index of refraction initiate scattering of the signal. If the electromagnetic signal has a wavelength of about one-half the size of the eddy, where wavelength is defined as the distance between two crests of the wave along its direction of motion, the electromagnetic signal is preferentially scattered back toward the profiler, or backscattered. If this backscattering eddy has a component of motion toward or away from the radar (also known as the radial component of the velocity), the return signal's frequency will be Doppler shifted by an amount proportional to this velocity. A Doppler frequency shift is the difference in frequencies between the transmitted and returned electromagnetic signals. From this difference, the radial velocity of the target can be deduced. From Huschke (1959) we have the Doppler equation: $f' = \frac{f}{1 \pm \frac{v}{c}}$, where f is the actual frequency at which the wind profiler transmits, f' is the shifted return frequency, v is the radial velocity of the detected eddy, and c is the speed of light. Police "radar guns" used for measuring automobile speeds operate on this same principle. For the case of our profiler, the electromagnetic signal propagates straight up. Thus if the eddy were moving up or down, any return signal generated would be Doppler shifted, and from this Doppler shift the speed of the eddy's vertical motion would be calculated by the profiler's processing system. It is assumed that the eddies in the air move with the wind. Thus by determining the vertical velocity of an eddy one also determines the vertical velocity of the wind. The overall wind field generally has horizontal motions as well as vertical motions, but after sampling return signals from the vertical direction, only the vertical motion of the air has been determined. In order to calculate the three-dimensional wind vector, radial velocities from the north-south and east-west directions must also be determined. After the vertical wind has been determined, the profiler transmits another signal, this time to the north, but at an elevation angle of about 75° above the horizon. Once the radial velocities to the north are determined, the process is repeated to the east, again firing the beam at a 75° elevation above the horizon. After the radar has sampled the wind in these three

directions, the profiler's processing system then determines the three-dimensional wind vector. Some wind profilers transmit beams to the north and south as well, since the additional information thereby gained leads to more accurate wind calculations. A wind profiler and its beam configuration are shown in figure 2.7.

A profiler has a maximum range of wind detection as well as a minimum range. A profiler's transmitted pulse is not completely scattered when it encounters an eddy, and in fact most of the pulse's energy will survive an encounter and continue to travel away from the profiler and encounter more eddies at various vertical levels. Eventually the pulse will exceed the profiler's range, but below this altitude of maximum range the profiler can determine three-dimensional wind vectors at many levels. The profiler's maximum range is proportional to the average power transmitted, the size of the profiler's antenna, and the turbulence of the atmosphere being investigated. The wavelength of the transmitted pulse also determines vertical range. As mentioned above, an eddy whose diameter is approximately twice the wavelength of the profiler's signal will be detected. Eddies of various sizes tend to be grouped at preferred heights, however. Since smaller eddies (of diameters on the order of a centimeter) are abundant only at the lower levels of the atmosphere, a profiler using a short wavelength would not detect eddies higher in the atmosphere which tend to be larger. Profilers also have a minimum vertical range below which they are blind. Wind profilers transmit a pulse of electromagnetic radiation and then wait to receive return signals. The profiler's receiver must be disconnected during pulse transmission to avoid circuit overload and is reconnected only after pulse transmission is completed. During the brief time in which the pulse is traveling but the receiver has not yet been turned on, backscattered energy from eddies at the lowest elevations strikes the receiver without being detected. Profilers thus are blind to winds below a certain elevation, and that elevation depends on the pulse length and the speed at which the profiler reactivates its receiver after transmission.

A profiler's resolution, i.e. the minimum separation at which two targets within the same beam can be discriminated, is related to the length of the radar pulses it transmits. Long pulses are desirable since received echo strength is proportional to pulse length, but

long pulses limit resolution. If the pulse were transmitted for an infinitely short duration, and thus were of an infinitely short length, we would know the exact altitude of an eddy which backscattered the pulse upon receiving the return echo since we would know the speed of the pulse (the speed of light) and the time elapsed between pulse transmission and echo reception. However, the pulse does have a certain length. Targets separated by a distance of less than half a pulse length cannot be discriminated since echoes received from the rear edge of the pulse as it passes targets at range r will be received simultaneously with echoes from the leading edge of the pulse passing targets at range $r + \frac{h}{2}$ where h is the pulse length. Thus the finest vertical resolution of a wind profiler is equal to one half the pulse length. Figure 2.5 illustrates the relationship between pulse length and resolution. The range gating process insures that echoes are interpreted properly. During range gating, echoes are sampled at equally-spaced times, or at "gates," as shown in figure 2.6. To insure that the samples are independent of each other, the sampling interval is equal to the resolution. A longer pulse leads to coarser resolution and widely-spaced range gates.

Consult Peterson (1988) for a more complete introduction to the principles of wind profiling.

Colorado State University provided the Porto Santo site with a Tycho Technology Model 400 wind profiler, which transmitted at a frequency of 404.37 MHz. This frequency is considered an "all weather" frequency since it is not sensitive to clouds and is rarely contaminated by precipitation. 404.37 MHz corresponds to a wavelength of 0.742 meters, and thus eddies roughly 1.5 meters across were best detected by the CSU profiler. The CSU profiler transmitted in five directions as opposed to only three: one beam was fired at the zenith, and beams were fired 15° off the zenith in each of the four compass directions. While scanning in each of these five directions, the profiler operated in high and low modes. The high mode scanned heights from 7.5km above ground level (AGL) to 16.25km AGL at a resolution of 1000m, and the low mode scanned heights from 500m AGL to 9.25km AGL at a resolution of 250m. The profiler scanned in one direction at a time, and each beam required two minutes' scanning to cover its high and low modes. Ten minutes were

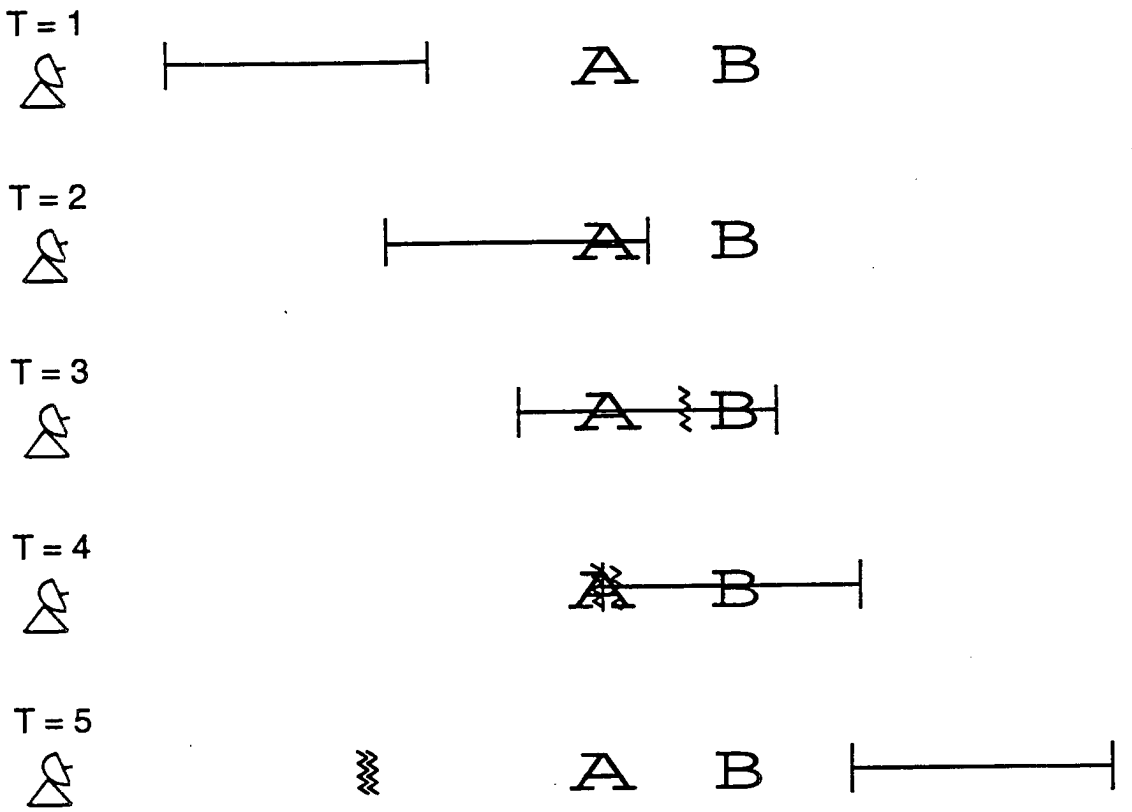

Figure 2.5: Relationship between pulse length and resolution. A radar and its pulse are depicted in five "snapshots." At time $t = 1$ the radar has just transmitted its pulse, and the pulse is approaching two targets, labeled A and B. Targets A and B are separated by a distance equal to one half the length of the approaching pulse. By time $t = 2$ the front of the pulse has passed and missed target A. By time $t = 3$ the front of the pulse has passed target B, and target B has reflected the front of the pulse. This reflection, denoted by the squiggle, is heading back to the radar. Note that the front of the pulse and the return signal are at equal distances from target B, illustrating that the speed of the return signal is equal to the speed of the original pulse. At time $t = 4$ the back of the pulse is passing point A, and point A is generating a reflection, denoted by another squiggle. At the same time, the reflection generated by target B is passing target A on its way back to the radar. The reflections are thus on top of each other, but to clearly illustrate that there are two return signals, the squiggles are separated slightly in this figure. By time $t = 5$ the entire outgoing pulse has passed both targets and is no longer a concern. The two reflections, one generated by target A and the other generated by target B, are heading back to the radar and will strike the radar simultaneously. The radar will not be able to discriminate between the two pulses. Thus one can never determine the location of a detected target more precisely than saying the target lies within a distance equal to one-half the length of the emitted pulse.

PARAMETERS	SHORT DESCRIPTION
ANT_DIR	Antenna direction
ARA	Anti-range aliasing for each mode
CCP_GAIN	Digital gain of the real and quadrature channels with the A/D converter
CODE	Complementary coding for each mode
CON_DELTAV	Consensus velocity half-width (m/s)
DELAY	Delay from fall of TX pulse to first range gate (1/6 μs)
DODC	Enables DC removal
DOPOWCOR	Corrects signal power values due to the range dependent attenuation of the T/R switch
FILTER	Receiver filter for each mode
GCNUM	Number of points around zero used in ground clutter removal (same for all modes)
POW_FACTOR	Power scaling factor
PRP	Pulse Repetition Period (0.1 μs)
PW_BAUD	Pulse width for each mode (1/6 μs)
RX_DELAY	Receiver delay (0.01 μs)
RX_GAIN	Receiver gain
SAMPLE_MIN	Minimum number of agreeing samples for consensus
SPACE	Time between range gates for each mode (1/6 μs)
SPAN	Number of spectral points around zero that are searched for peak power
SPECTRA	Number of spectra averaged for each data-taking mode
SSTDODC	Enables SST DC-removal
TDA	Number of samples per time domain average for each mode
WINDOW	Enables a HANN windowing function for the FFT

Table 2.3: List of the operator-selected parameters determining the operating charcteristics of the CSU wind profiler. From Cox et al. (1993).

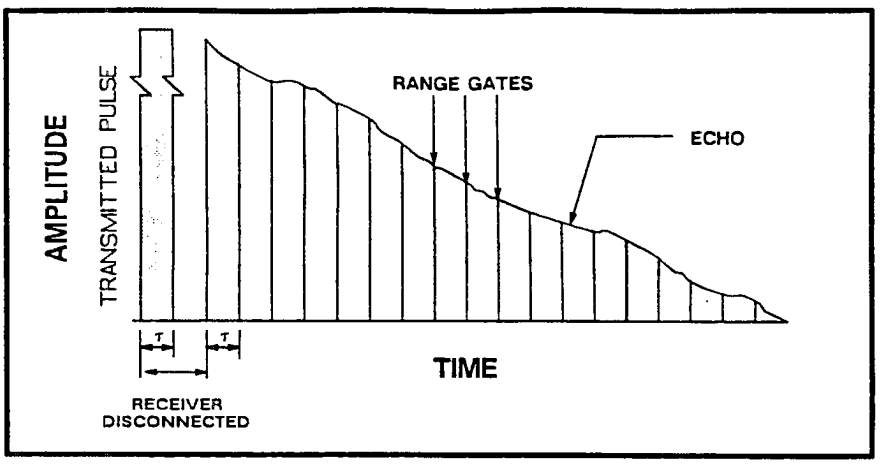

Figure 2.6: Range gating. After each pulse is transmitted, the echo is sampled at selected times, or range gates. The echoes recieved between gates are ignored. From Peterson (1988).

thus required to completely sample the wind field. The profiler's processing system then required two minutes to process and down-load the gathered data, thus bringing total time required for a complete cycle to twelve minutes.

The CSU profiler also served as part of CSU's radioacoustic sounding system (RASS). RASS acquires a temperature profile of the boundary layer by emitting an audio signal from speakers at the ground station and tracking the signal's acoustic wavefronts as they propagate upward through atmospheric layers of varying temperature. A wind profiler is an important part of this system, and RASS frequently diverted the profiler from its wind sensing routine. The profiler was often being used for RASS during times when it would have normally been scanning the wind field to the west and south. Since scans to the west and south were inconsistent or incomplete, winds were calculated using the vertical, north, and east scans only.

Wind profiler data are included in this paper to be compared to radiosonde wind data, and since a radiosonde's complete ascent requires roughly one hour, radiosonde wind profiles will be compared to hourly-averaged wind profiler data. As mentioned above, the wind profiler took twelve minutes to scan and process the three-dimensional wind field. Thus five scans were made each hour. The averaging algorithm used on the profiler data

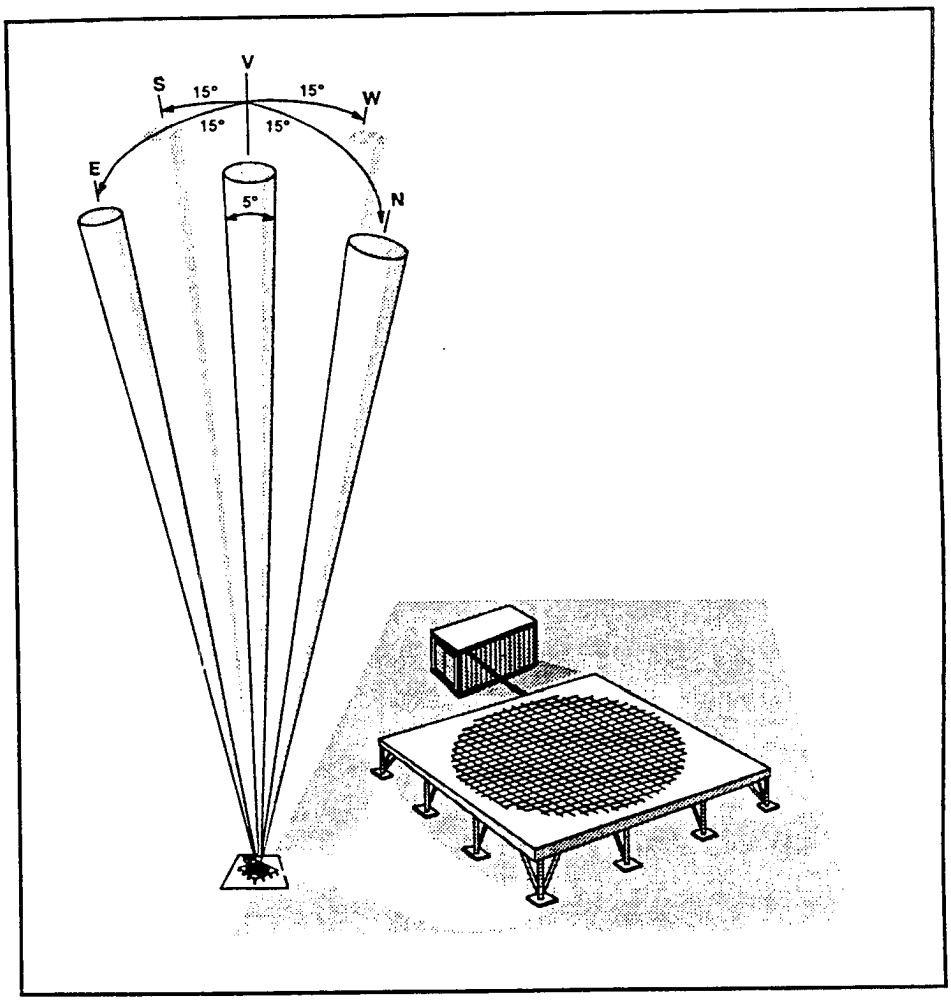

Figure 2.7: The CSU wind profier sampled radial velocities by transmitting five beams: one vertical, and four tilted 15° from the zenith toward the north, east, south, and west. From Peterson (1988).

examined the radial velocity value at each vertical gate of each beam. The averaging algorithm required that at least three of the five values at each gate agree well with each other, otherwise no averaging was performed and a value of zero was recorded as that gate's hourly average. Outlying data were eliminated by the algorithm, and occasionally entire scans were missed because the profiler had been shut down when satellites passed over Porto Santo. Once the hourly-averaged values of radial velocity had been calculated at each gate of each beam, the hourly-averaged three-dimensional wind vectors at each gate were calculated. The following algorithm, based on an algorithm by Tycho Technology, Inc., was used to calculate the wind vectors:

$$V_{re} = -u \sin 75° - w \cos 75° \tag{2.14}$$

$$V_{rn} = -v \sin 75° - w \cos 75° \tag{2.15}$$

$$V_{rz} = -w \tag{2.16}$$

where V_{re}, V_{rn}, and V_{rz} are are radial velocities measured in the east, north, and zenith directions, respectively, and U, V, and W are the east-west, north-south, and vertical components of the wind vector. These equations assume the wind flow is horizontally homogeneous between the beams. Therefore only wind fields with details on a scale at least as large as the distance between the off-zenith beams can be calculated. This "horizontal resolution" becomes cruder toward higher altitudes. For example, for a gate at 1km AGL the horizontal resolution is 0.38km while for a gate at 10km AGL the resolution is 3.8km, and so on. The above equations also assume the wind field does not change significantly during the hour over which the original data were collected.

After the three-dimensional wind vectors were calculated at each vertical gate, a correction was made in their horizontal orientation. When the CSU profiler was assembled at the Porto Santo site, an error was made in correcting for the 9° deviation between magnetic north and true north, and the net result was a profiler pointing 18° counter-clockwise from true north. Since the profiler was assumed to be pointing toward true north, the wind vectors calculated from the profiler's data needed correcting by 18° in the horizontal plane. Some gates were then eliminated from the final data set. Gates whose

vertical velocities were greater or less than $2ms^{-1}$ were classified as unreasonable in a stratocumulus environment and were removed. Also, any gate having a u or v component of exactly zero was removed. Such zero values were probably generated by the hourly-averaging algorithm when it failed to find three radial velocities out of five which closely agreed. In both of the above cases a single bad component was cause enough to throw out a gate's entire wind vector, given the interdependence of the components shown in equations (2.14-2.16). A vertical velocity value of exactly zero was not considered grounds for eliminating a gate since vertical velocities were generally small in the Porto Santo environment. Table 2.4 presents a sample of Porto Santo wind profiler data in its final form.

The ASTEX data set contains hourly-averaged radial velocities V_{re}, V_{rn}, and V_{rz} at all range gates for each of the 203 hours during which a radiosonde was launched. From these radial velocities, three-dimensional wind vectors were generated and the resulting 203 files were all cleaned as described above.

2.3 Doppler Cloud Radar

A cloud radar differs from a conventional weather radar. Such a radar is called a "cloud radar" because, unlike conventional radars which detect only cloud particles large enough to be falling from clouds as precipitation, a cloud radar's frequency allows detection of cloud particles too small to precipitate out of a cloud; in effect, a cloud radar detects the clouds themselves as well as any precipitation they may produce. During moderate or heavy precipitation events, however, cloud radars suffer a loss of signal as the radar beam has difficulty penetrating through a volume filled with so many large particles.

The Wave Propagation Laboratory (WPL) of the National Oceanic and Atmospheric Administration's Environmental Research Laboratory provided the Porto Santo observation site with a Doppler cloud radar. The WPL radar transmitted at a frequency of 34.6 GHz, which lies within the K_α radar frequency band and corresponds to a wavelength of 8.7 mm. The radar sampled return signals from 328 range gates spaced at intervals of 37.5 m, yielding a maximum range of 12.3 km. The WPL cloud radar was also a Doppler

PRESSURE(MB)	U (M/S)	V(M/S)	W(M/S)
931.0174	1.8493	1.6314	-.1960E+00
897.8950	3.3420	2.0506	-.1440E+00
865.9506	4.0400	.7725	-.2200E+00
835.1429	6.2395	-.4199	-.5800E-01
805.4315	10.0656	-.2969	-.1000E-01
776.7766	11.8435	-1.6775	.2200E-01
749.1416	12.5341	-1.3759	-.1700E+00
722.4894	12.6265	-.2644	-.1180E+00
696.7856	11.1337	-.2946	-.5200E-01
671.9961	11.1845	.3941	-.2000E-01
648.0887	10.7696	-1.0477	-.4000E-01
625.0317	9.7769	-.7723	-.7600E-01
602.7952	10.3902	-1.9173	-.8600E-01
581.3495	10.7753	-2.0923	-.5600E-01
560.6671	10.0148	-2.3549	.1800E-01
540.7202	9.7041	-2.3933	.2200E-01
521.4833	9.9505	-2.6059	.6200E-01
502.9307	11.2062	-2.9450	.8600E-01
485.0379	10.3874	-2.0523	.1200E-01
467.7819	10.5567	-1.8440	-.2000E-02
451.1396	11.4751	-2.7150	.1200E+00
435.0896	13.3381	-3.4738	.8800E-01
419.6104	12.8834	-3.0960	.6200E-01
404.6821	11.3675	-3.6240	.7000E-01
390.2847	10.5459	-3.3719	.3400E-01
376.3997	10.0741	-3.3302	-.4000E-02
367.6138	12.2900	-1.7659	-.6540E+00
363.0085	10.3746	-6.2583	-.8600E-01
354.5352	10.9073	-4.3856	-.4000E+00
350.0939	10.2383	-7.1959	-.1367E+00
341.9221	10.9647	-6.6620	-.4567E+00
337.6388	8.6753	-10.8050	-.5200E-01
329.7576	11.5555	-8.4674	-.5000E+00
325.6266	12.9705	-11.8518	-.1150E+00
318.0258	13.0726	-8.6327	-.6733E+00
314.0419	15.0228	-11.8715	-.1367E+00
306.7116	13.5846	-9.4899	-.4267E+00
285.2762	12.9726	-7.7952	.0000E+00
275.1269	12.6420	-6.4805	.0000E+00
265.3388	13.2352	-6.2782	.0000E+00
262.0149	12.6549	13.9386	.0000E+00
255.8990	13.2060	-5.4652	.0000E+00
246.7948	13.2838	-6.3534	.0000E+00
198.5829	14.2368	-4.4992	.0000E+00
171.7959	24.5448	-5.2513	.0000E+00
165.6839	25.2761	-5.7310	.0000E+00
133.3172	35.2678	-4.0584	.0000E+00

Table 2.4: A sample of wind proiler data in its final form from June 28, averaged over the hour 1700Z to 1759Z. A positive w component corresponds to downward motion, a positive v component corresponds to flow from the south, and a positive u component corresponds to flow from the west.

radar, and thus it determined the radial velocities of the particles it detected. As noted by Martner, et al. (1993), the WPL radar produces very detailed images of cloud location and structure, even for multiple cloud decks. The power in the radar's side lobes is weak compared to that of other radars, and thus ground clutter is only a minor problem. Figure 2.8 shows a picture of the K_α-Band cloud radar used at Porto Santo, and table 2.5 is a complete list of the operating characteristics of this radar. For a more detailed description of the WPL cloud radar, consult Martner, et al. (1993).

Upon detecting a cloud or cloud and precipitation, the WPL radar generated output products showing Doppler velocity and reflectivity. Doppler velocity was determined by measuring the Doppler shift in return signal frequency in much the same way that the wind profiler determined radial wind component velocities. Whereas the wind profiler sampled air movement from the zenith and at least two other directions 15° off the zenith to capture the three-dimensional flow of the wind, the WPL radar scanned almost exclusively toward the zenith, in fact, all Doppler velocity data presented in this paper were generated with the WPL radar pointing straight up, or in vertical mode. The radial velocities measured by this method are thus equivalent to updrafts and downdrafts; horizontal motions of the cloud particles were not captured by the vertical mode. A sample of Doppler velocity output is show in the top half of figure 2.9. While the WPL radar gathered Doppler data, it simultaneously gathered reflectivity data. Reflectivity is a measure of the fraction of the radar's outgoing signal that is reflected back to the radar; the larger and more numerous the cloud particles or precipitation particles detected, the larger the reflectivity. A sample of reflectivity output is shown in the bottom half of Figure 2.9. For the purposes of this paper, the WPL radar's determinations of cloud base and cloud top are most important. Figure 2.10 shows a simplified version of the radar's output in which only cloud base and cloud top are displayed. It is important to remember when looking at all of these figures that the WPL radar's measurements of heights are in meters *above the radar.* Since the Porto Santo observation site had an elevation of 97 meters above sea level, 97 meters must be added to the radar's height calculations when comparing radar data to other height data based on elevation above mean sea level.

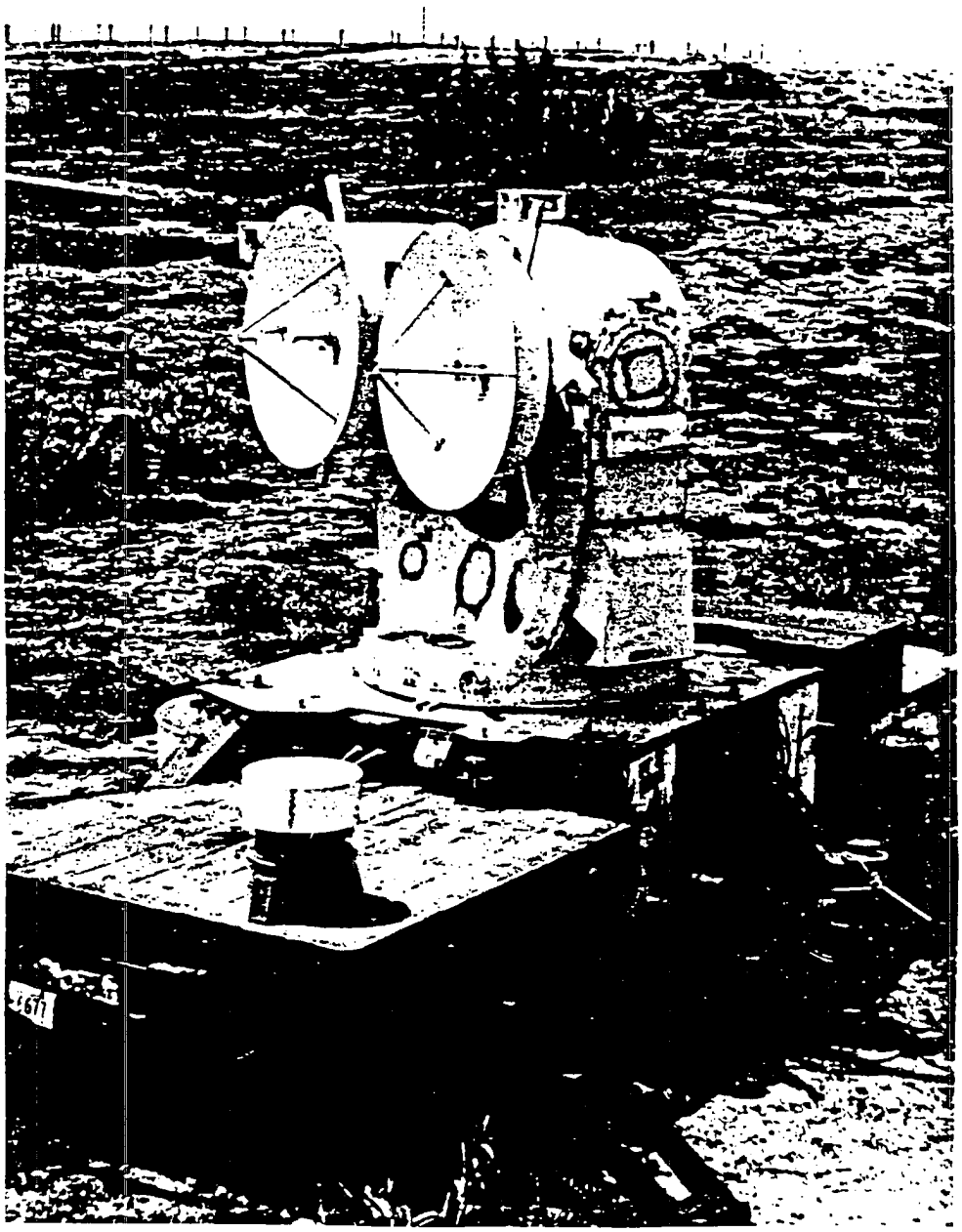

Figure 2.8: The K_α-Band antenna used during ASTEX. From Cox et al. (1993).

Major capabilities:	reflectivity, velocity, and depolarization for atmospheric research, including observations of non-precipitating clouds
Frequency:	34.6 GHz - 8.7 mm wavelength (K_α-band)
Peak transmitted power:	85 kW
PRF:	2.0 KhZ (double pulse mode)
Sensitivity:	approximately -30 dBZ at 10 km
Polarization:	circular
Beam Width:	0.5° circular
Antenna:	Bistatic center-fed Cassegrain with two 1.2 m diameter parabolic dishes; gain approx. 47 dB
Scan Types:	PPI (incl. sector scans), RHI (incl. over the top), zenith, fixed beam
Pulse width:	fixed, 0.25 μs (37.5 m)
Range gate spacing:	(n)*(37.5 m) where n = 1, 2, 3 ...
Number of range gates:	328
Scan rates:	0-30 deg/s; fastest rate depends on sector size
Parameters measured:	reflectivity (main- & cross-polarized), mean Doppler velocity, variance of Doppler spectrum, circular depolarization ratio (CDR), correlation of successive pulses, full Doppler spectrum in a separate recording mode
Doppler processing:	Data General S-120 computer controls antenna operation, recording and displays through NOAA's Radar Control Program. Hundreds of pre-programmed scans can be retrieved from disk for immediate use. SUN workstation for post-processing in field.
Recording:	Exabyte 8mm video cassette tape drives. VCR used for recording visual weather in direction of radar beam. PC electronic logbook for operator's comments.
Real-time displays:	color monitor of Doppler velocity, reflectivity, CDR and correlation patterns; Video monitor of weather along beam; digital displays of azimuth, elevation, and time; field tapes can be played back through color monitor.

Table 2.5: Characteristics of the NOAA/WPL K_α-Band radar. From Cox et al. (1993).

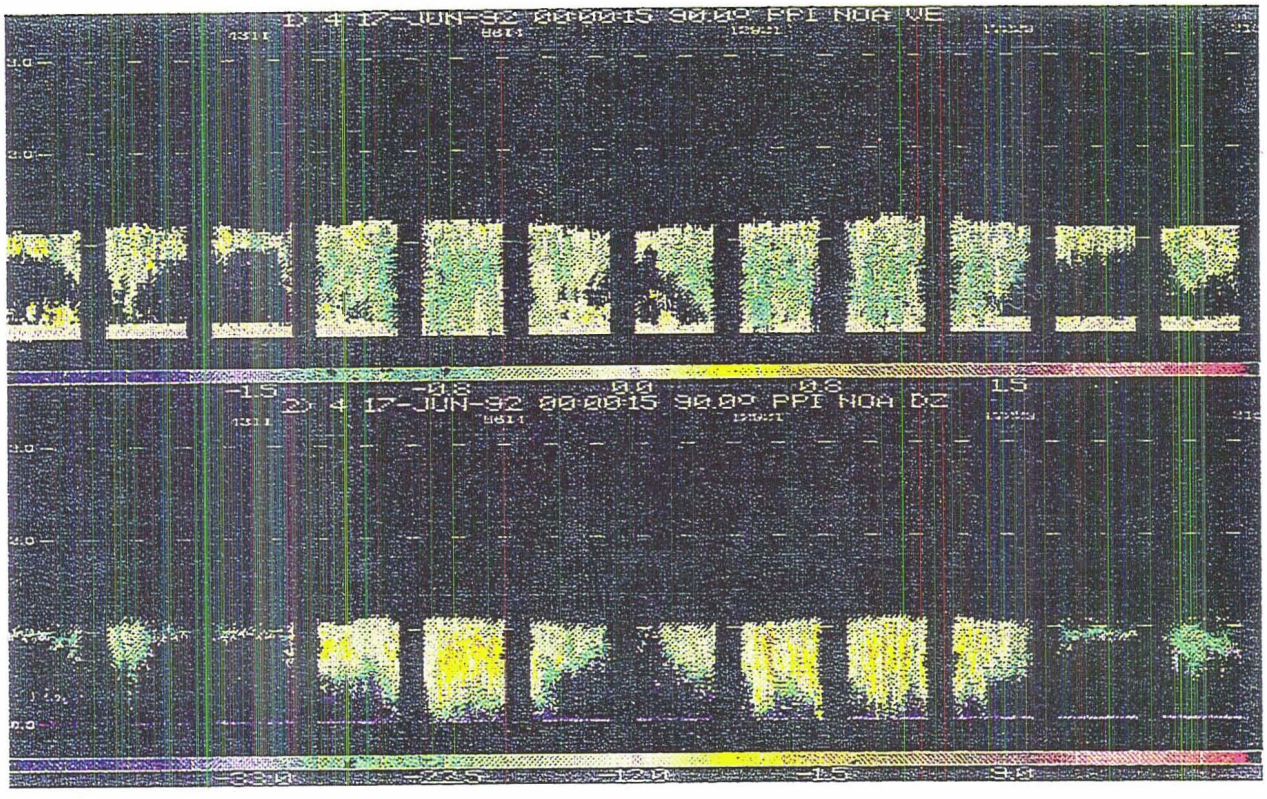

Figure 2.9: Sample output of the WPL K_α-Band radar. The top half of the figure shows Doppler velocity output for June 17th between 0 and 6 UTC, with height in kilometers as the vertical axis and time as the hortzontal axis. Velocities and their corresponding colors are defined on the color band below the data. Negataive values correspond to downward motion, and positive values correspond to upward motion. Units are ms^{-1}. The lower half of the figure shows reflectivity output for the same perid, with the axes the same as in the Doppler velocity plot. Reflectivities are in units of dBZ, with higher values corresponding to higher reflectivities and thus to heavier precipitation or "thicker" clouds. The occasional gaps in the data represent times when the radar was operating in a non-vertical mode.

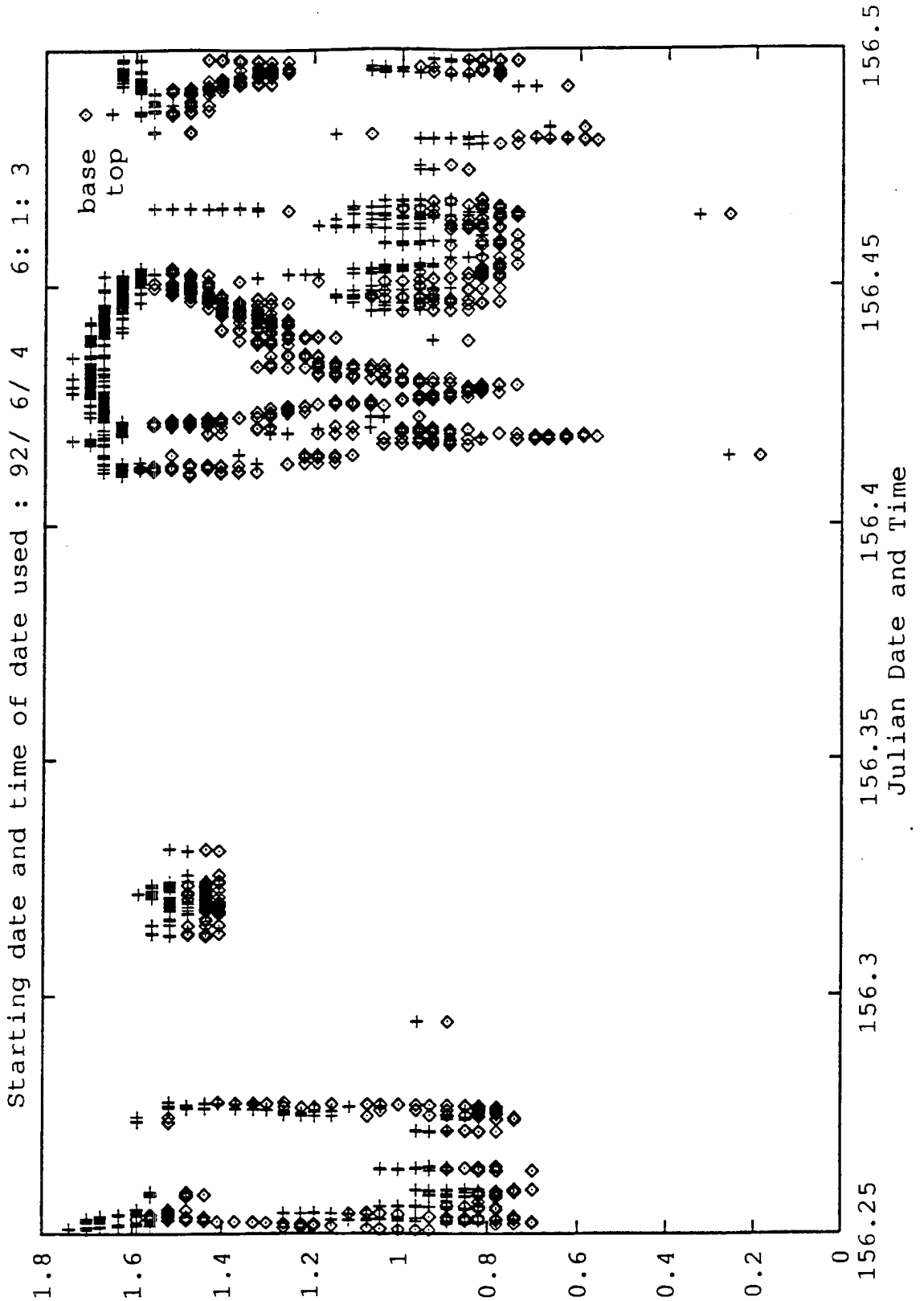

Figure 2.10: Doppler radar calculations of cloud base, denoted by $\diamond$, and cloud top, denoted by $+$. The vertical axis shows kilometers above the radar, and the horizontal axis displays time, where the number to the left of the decimal is Julian date, and the number to the right of the decimal is fraction of day. Thus this plot spans the hours from 6am to noon on June 4th.

The ASTEX data set includes representations of Doppler velocity and reflectivity (like the data shown in figure 2.9) for the entire ASTEX period, June 1 through June 28. In addition, files containing simplified output, as shown in figure 2.11, were generated for the entire ASTEX period.

2.4 Laser Ceilometer

A laser ceilometer system determines a cloud base's height above the ground. The system consists of three components: (*a*) the transmitter, which fires a laser pulse toward the zenith; (*b*) the detector, which receives any portion of the pulse's energy which is reflected back to earth after striking a cloud base; and (*c*) the recorder, which amplifies the return signal, thus helping it stand out against background light. The height of the cloud base, or the height of the ceiling, is calculated using the speed of the laser pulse, which is the speed of light, and the time elapsed during the pulse's ascent and descent. If the sky is clear, the laser pulse passes out to space, and no return signal is registered. Like the wind profiler and cloud radar, a ceilometer uses range gating when interpreting return signals, and the instrument's resolution is equal to one-half its pulse length.

The ceilometer used at Porto Santo was a Belfort Laser Ceilometer. It fired a 20 watt near-infrared Gallium-Arsenide laser at a wavelength of 0.91 μm. The system sampled the return signal at 1024 range gates spaced at 25 foot intervals, yielding a maximum vertical range of 25,600 feet. The fields of view of both the transmitter and receiver were approximately one degree. In a 1986 intercomparison, Oulridge et al. (1989) found that the Belfort model had a lower detection rate than other ceilometers, but that when the Belfort detected a cloud its calculation of cloud base height agreed closely with the median cloud base height determined from measurements made by the entire group of ceilometers. Two Belfort ceilometers were used at the intercomparison, and their distributions of reported heights were identical within the resolution of the instrument. We will thus assume that the ceilometer used at ASTEX had the same performance characteristics as those used in the intercomparison.

Each time the ceilometer at Porto Santo took an observation, which was once every minute, the following procedure was observed. The ceilometer first, before firing the laser,

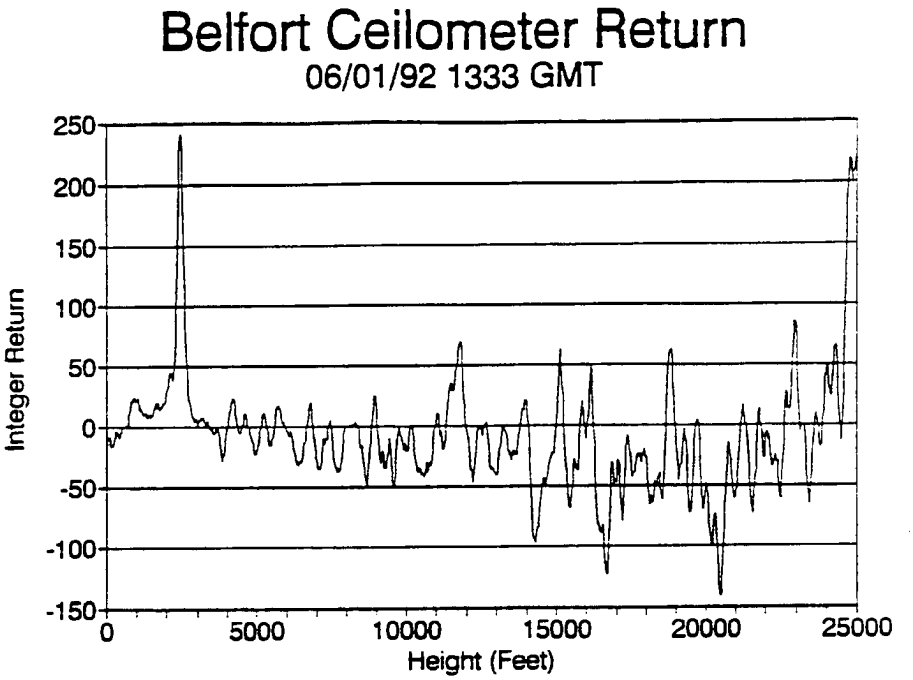

Figure 2.11: Histogram of ceilometer output from 1333 GMT, June 1, 1992. The cloud base is about 2500 feet above ground. Note that not even 250 of the 5120 laser firings yielded a detection of cloud base at 2500 feet, yet 2500 feet is clearly the cloud base height. The ceilometer's laser is fired many times in order to obtain a consensus estimate of cloud base height, since there would be too much variability in relying on only one or a few firings. From Cox et al. (1993).

sampled all 1024 range gates three times to establish background noise levels. Then the laser was fired 5120 times, and the reflected signal was sampled after each firing. After every sampling, the sampled signal from each range gate was compared to that gate's established background value. Depending on whether the sampled signal was above, below, or within the established noise level band, integer values of 1, -1, and zero, respectively, were assigned to the gates. After all 5120 laser firings and return signal samplings, the integer values were summed for each gate. Figure 2.11 shows a sample of these summations displayed in histogram format.

The data, like those shown in figure 2.11, were then run through a firmware peak-location algorithm (designed by J.D. Klett and described in Klett (1991)) to obtain a first order estimate of ceiling height. The ceiling heights were also converted into units

of meters during this process. For more information regarding the processing of the laser ceilometer's return data, consult Klett (1981) and Klett (1986). Table 2.6 shows a brief display of ceilometer data in its final form. The ceilometer's data can look erratic as the ceilometer oscillated between reading a clear sky and detecting a ceiling. The instrument's narrow field of view restricted it to sampling return signals from a small area directly overhead, and under patchy clouds rapid oscillations between reading a clear sky and detecting a ceiling are reasonable.

As in the case of the Doppler cloud radar, the ceilometer used at ASTEX measured the height of the cloud base *above the ceilometer.* Since the Porto Santo observation site had an elevation of 97 meters above sea level, ceilometer-calculated cloud base heights of 100 meters are actually 197 meters above sea level. The entire ASTEX data set contains uninterrupted one-minute ceilometer data from May 31 through June 29.

153.00000,	1784
153.00070,	-1
153.00140,	-1
153.00210,	-1
153.00280,	-1
153.00350,	-1
153.00420,	-1
153.00490,	-1
153.00560,	1715
153.00630,	1707
153.00690,	-1
153.00760,	1867
153.00830,	-1
153.00900,	1730
153.00970,	-1
153.01040,	1799
153.01110,	747
153.01180,	1806
153.01250,	-1
153.01320,	-1
153.01390,	-1
153.01460,	724
153.01530,	762
153.01600,	-1
153.01670,	-1

Table 2.6: Ceilometer data in its final form. The left-hand column represents time with Julian Date to the left of the decimal and fraction day elapsed to the right of the decimal. The second column displays ceiling height above ground in meters, where values of "-1" indicate a clear sky. Thus in the first row "153.00000, 1784" is read as June 1st, 12:00 midnight, cloud base height 1784m above ground. Row two is read as June 1st, 12:01am, clear sky. Since the ceilometer scanned the sky with a beam only 1° wide, oscillations between a ceiling reading and no ceiling reading indicate a patchy sky.

Chapter 3

DATA COMPARISONS

Once the ASTEX data were cleaned and in their final form, various instruments' wind calculations and calculations of cloud base and top were analyzed. Wind comparisons were made from data gathered by the radiosonde and the wind profiling radar. Overall, the radiosonde and profiler winds agreed in both their wind speed and wind direction measurements, and even small features in the wind profile were frequently detected by both instruments, especially at lower elevations where the wind profiler was at its most accurate. Data from the laser ceilometer, the Doppler cloud radar, and the radiosonde system were used in comparisons of cloud base and cloud top heights. Under very stratified conditions, the ceilometer and Doppler cloud radar agreed on the height of cloud base, and the Doppler cloud radar and the radiosonde agreed on the height of cloud top. At this same time the radiosonde often assigned lower heights to saturated layers than one would expect, given the ceilometer and Doppler cloud radar data. Under less stratified conditions, however, the ceilometer and cloud radar agreed less frequently, and there were instances in which one instrument completely missed a feature seen by the other.

3.1 Comparison of the Wind Data

Each of the 203 wind profiles generated by the radiosonde system during ASTEX was matched with its corresponding hourly-averaged wind profiler profile. All 203 comparisons cannot be shown in this paper due to space limitations, but several examples are presented.

Figure 3.1 compares the winds derived by the first ASTEX sonde launched at 02 UTC, June 1st and the corresponding hourly-averaged wind profiler data. In figure 3.1, as in all subsequent wind comparison diagrams presented in this paper, the wind has been split into two parameters: speed and direction. The left-hand panel of figure 3.1 displays

wind speed in ms^{-1}, with the solid line representing the sounding profile and the dashed line representing the wind profiler profile. The right-hand panel displays wind direction in degrees form true north. The degrees correspond to the direction the wind is blowing from; thus in figure 3.1 the wind is blowing primarily from the northwest at lower altitudes and from the west at higher altitudes. In both the left and right-hand panels, the vertical axis is height, measured in kilometers. A pressure axis is also included on the far right of the figure.

As mentioned in Chapter 2, the wind profiler's winds were averaged over one hour and then cleaned. The cleaning included removal of any range gate having a vertical velocity w greater than 2 ms^{-1}, but before 2 ms^{-1} was chosen as an appropriate cut-off value given Porto Santo's stratocumulus environment, vertical motions of up to 5 ms^{-1} were allowed to remain in the data set. A bad w wind tended to produce u and v winds which were unreasonable since the horizontal wind components were derived using the vertical component. Thus entire range gates had to be removed whenever w exceeded 2 ms^{-1}. Figure 3.2 shows a comparison between radiosonde and wind profiler winds for 02 UTC, June 1st, which is the same comparison shown in figure 3.1, but in figure 3.2 profiler range gates with vertical velocities of up to 5 ms^{-1} have been plotted. The plots of profiler wind speed and direction appear more jagged in figure 3.2 than in figure 3.1. Notice the bad data points in the profiler data between roughly 10 and 11 km in figure 3.2. These bad data appear at exactly the same altitude in both the wind speed and the wind direction plots. These spikes are the result of a bad data point, a range gate in which the w was greater than 2 ms^{-1} but less than 5 ms^{-1}. At higher altitudes the wind profiler returned a higher percentage of data points having w greater than 2 ms^{-1}, and thus the profiler plots became less detailed at these altitudes due to a lack of data points.

The radiosonde winds and wind profiler winds agreed quite well in both speed and direction. Figures 3.3 through 3.6 provide examples of this agreement. Notice that figure 3.4 also contains a bad wind profiler range gate at 9.5 km. Throughout the cleaned data set, bad wind profiler range gates which were not bad enough to be detected and deleted by the cleaning algorithm survived to be plotted in the comparison with radiosonde winds.

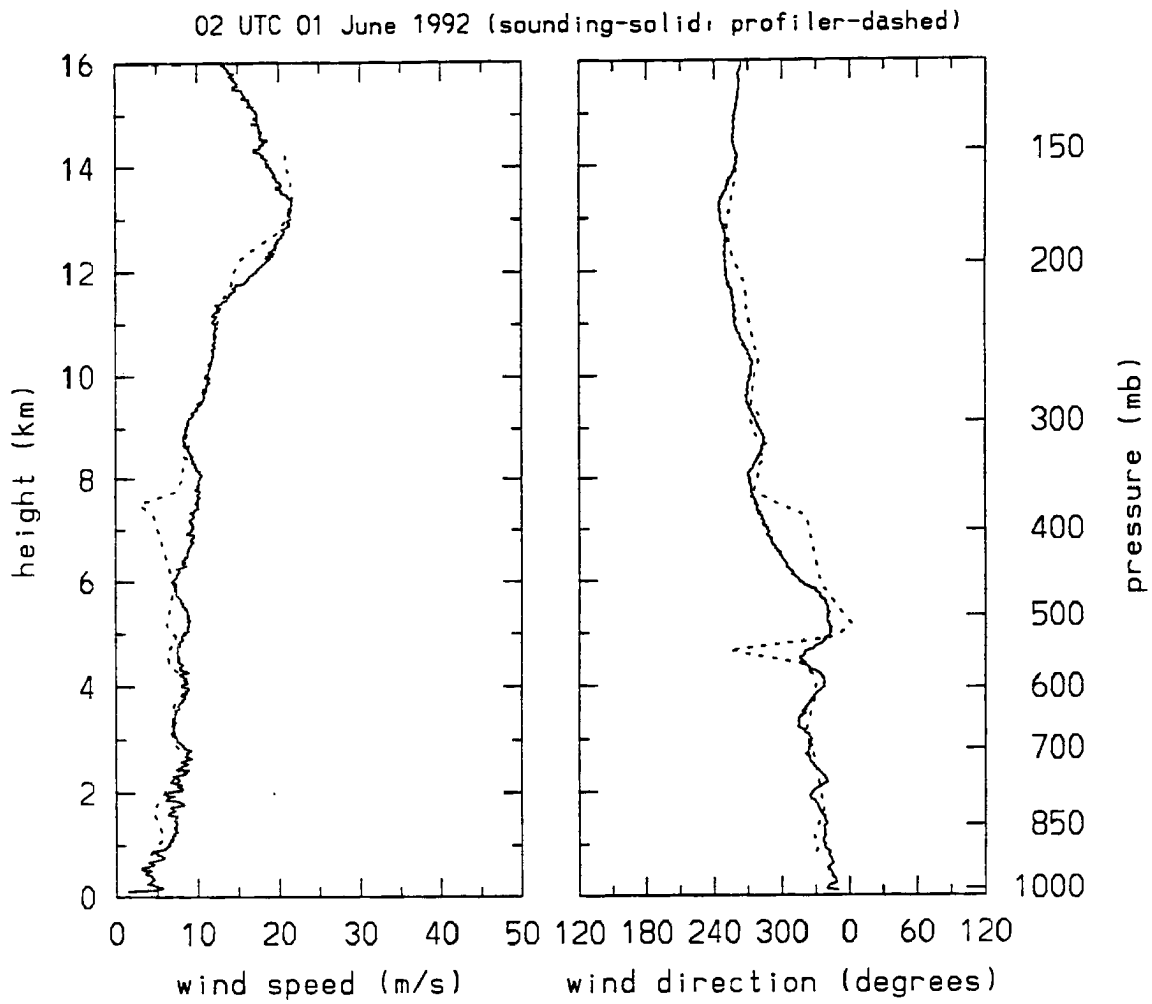

Figure 3.1: Comparison of wind data at 02 UTC, June 1st.

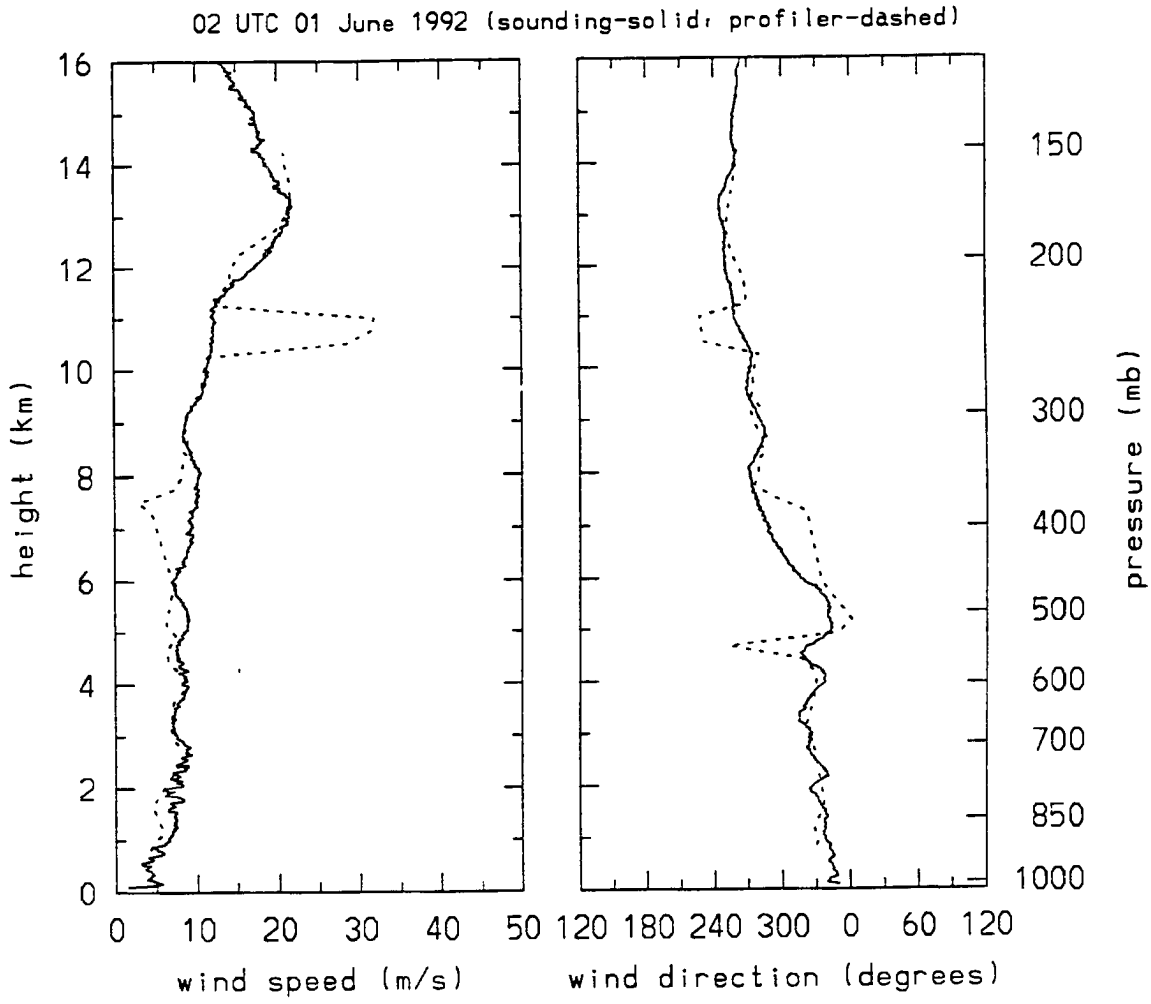

Figure 3.2: Comparison of wind data at 02 UTC, June 1st, allowing w up to 5 ms^{-1}. This figure displays the same radiosonde data as shown in figure 3.1, but fewer range gates have been removed during the cleaning of the wind profiler data.

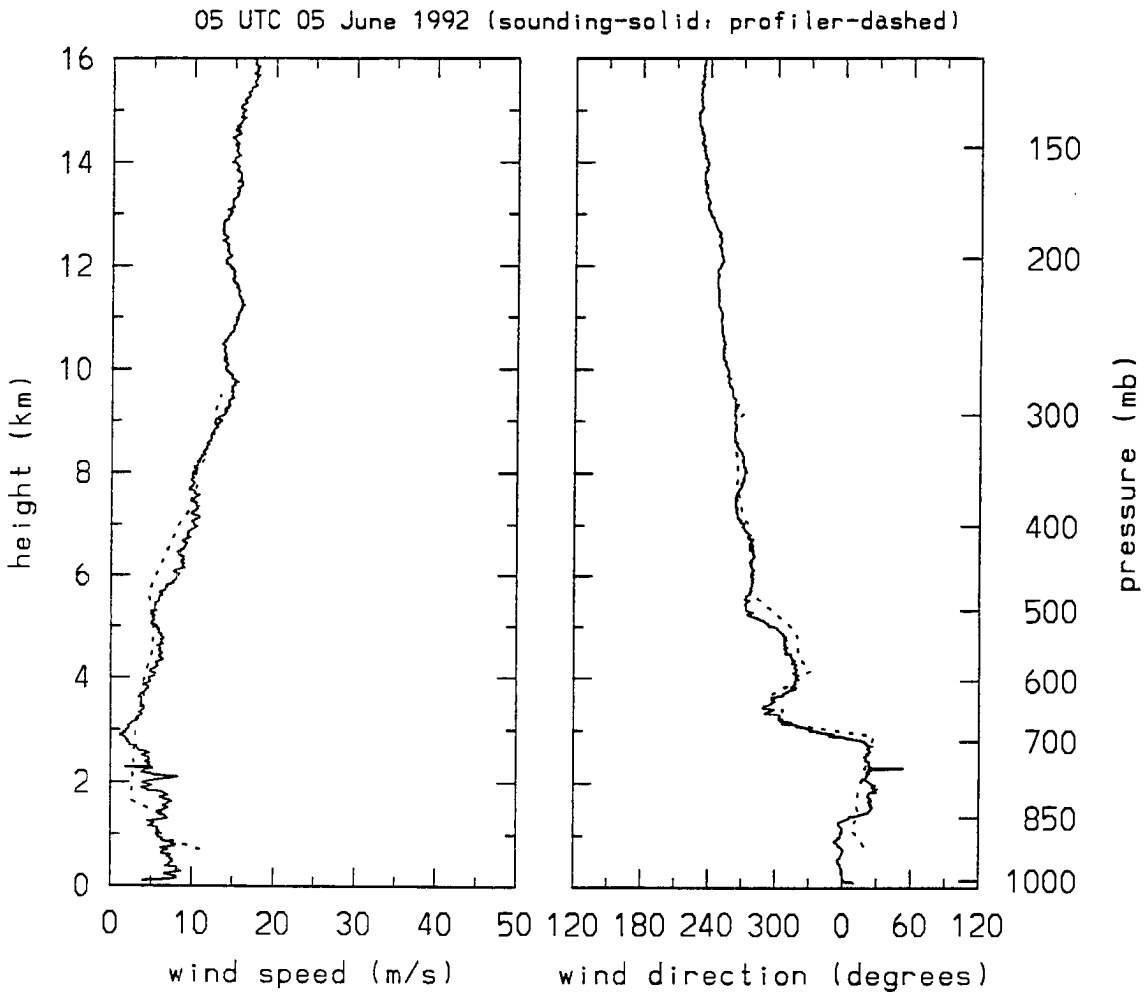

Figure 3.3: Comparison of wind data at 5 UTC, June 5th.

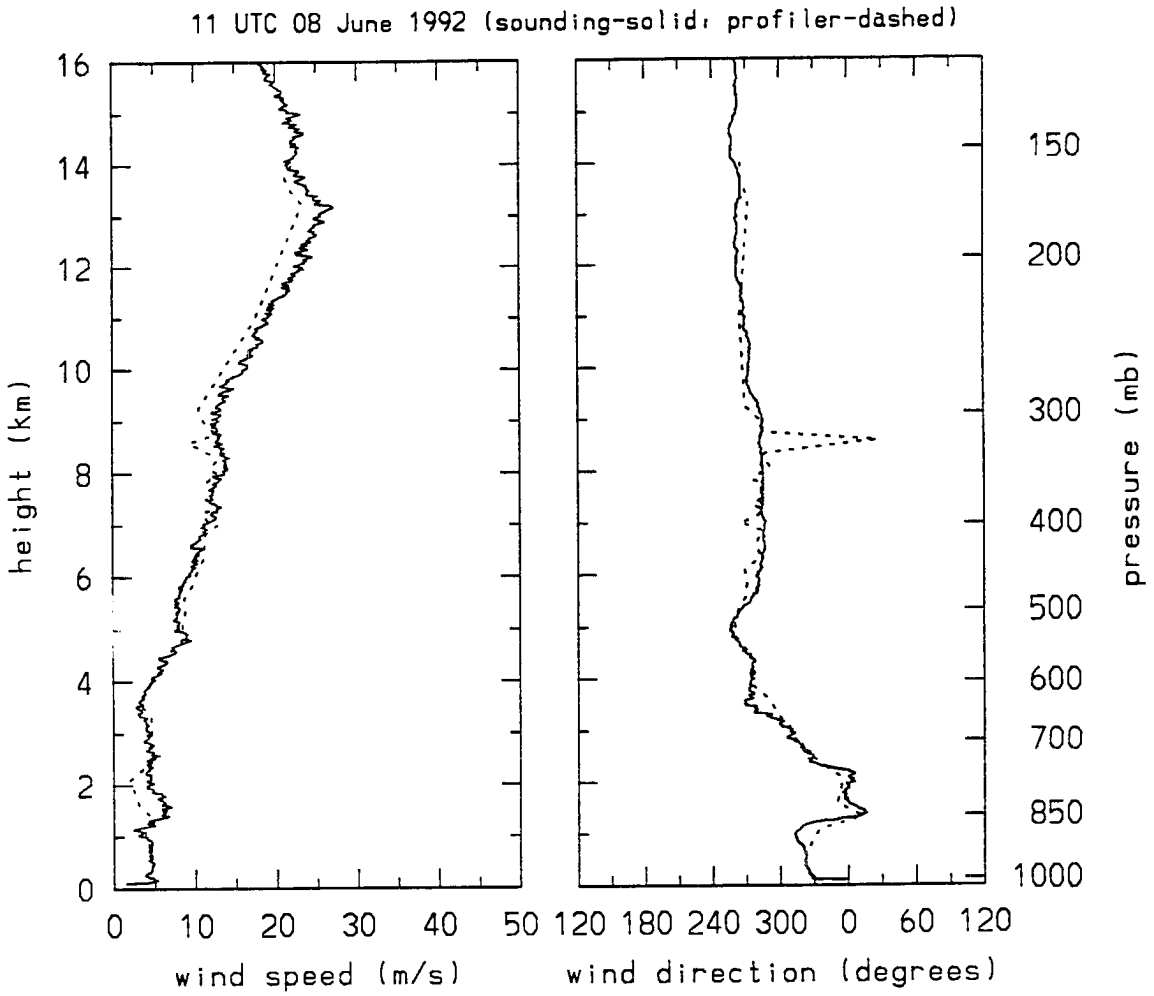

Figure 3.4: Comparison of wind data at 11 UTC, June 8th.

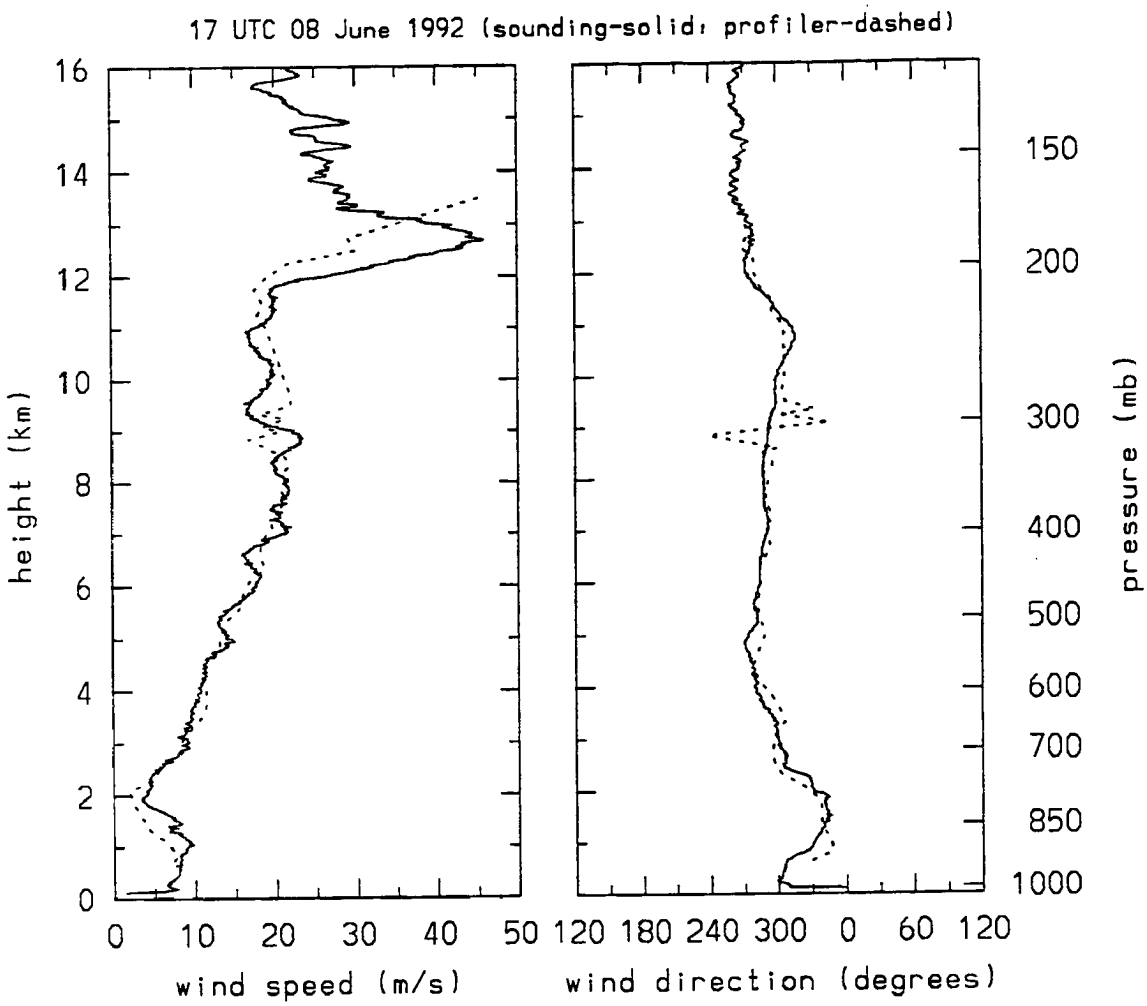

Figure 3.5: Comparison of wind data at 17 UTC, June 8th.

While these data points are obviously erroneous and could have been deleted manually after inspection of the comparison plots, the profiler data were left in their systematically-cleaned form; all wind profiler data were cleaned in the same way to preserve continuity of the data set and to avoid subjective manipulation.

The upper third of the wind speed plot in figure 3.7 shows how error-prone the wind profiler becomes at higher altitudes. Between 10 and 13.5 km there are no range gates which survived the data cleaning process, and the points at 10 km and 13.5 km are thus connected by a straight line. This courseness illustrates the dilemma encountered in cleaning the profiler data—at higher altitudes the profiler becomes less accurate and returns many unreasonable values, but a cleaning process that is too strict could eliminate good data along with bad data. Figure 3.8 presents a more extreme example of the wind profiler's high altitude inaccuracy. Above 10 km, the wind profiler just connects the dots, and a number of these dots are inaccurate in both speed and direction, although occasionally the wind profiler does come back to an agreement with the radiosonde. Wind profiler data again become thin toward higher altitudes in figure 3.9, and then the profiler data ends at 10.5 km. After the data in figure 3.9 were cleaned, no wind profiler range gates remained above 10.5 km. There were a few extreme cases in which none of the wind profiler's range gates survived to be plotted. The cause behind such cases was the hourly-averaging algorithm, which returned values of zero for all wind components at a range gate if a satisfactory average was not generated. When orbiting satellites flew over Porto Santo, the wind profiler had to be turned off. The resulting gap in an hour's data left the averaging algorithm no option but to assigning all range gates values of zero, and such range gates were deleted when the data were cleaned.

3.2 Comparisons of Cloud Base and Cloud Top Heights

All ceilometer, Doppler cloud radar, and radiosonde calculations of cloud base and cloud top were compared. Because of limitations on space, only a handful of examples of these comparisons will be presented in this paper.

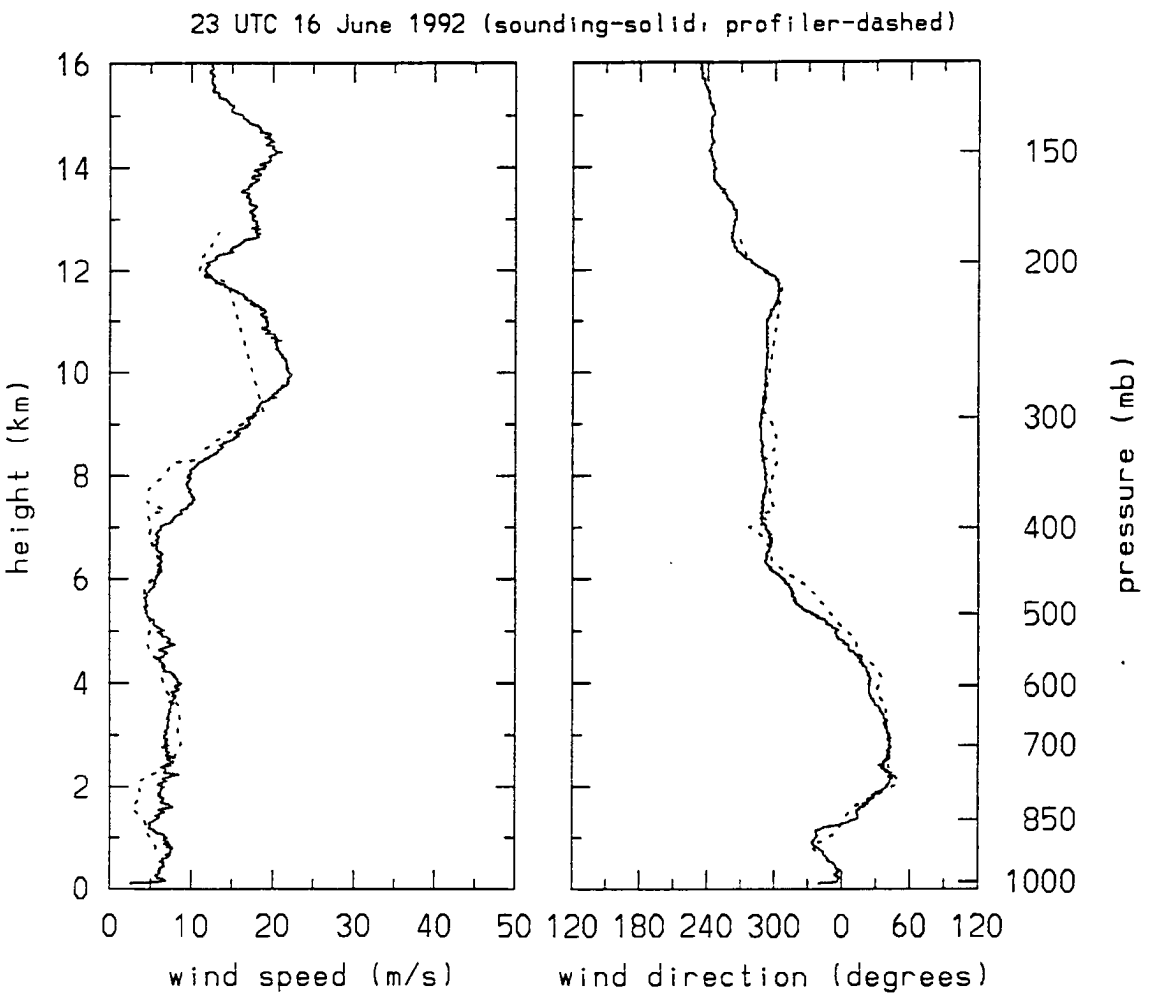

Figure 3.6: Comparison of wind data at 23 UTC, June 16th.

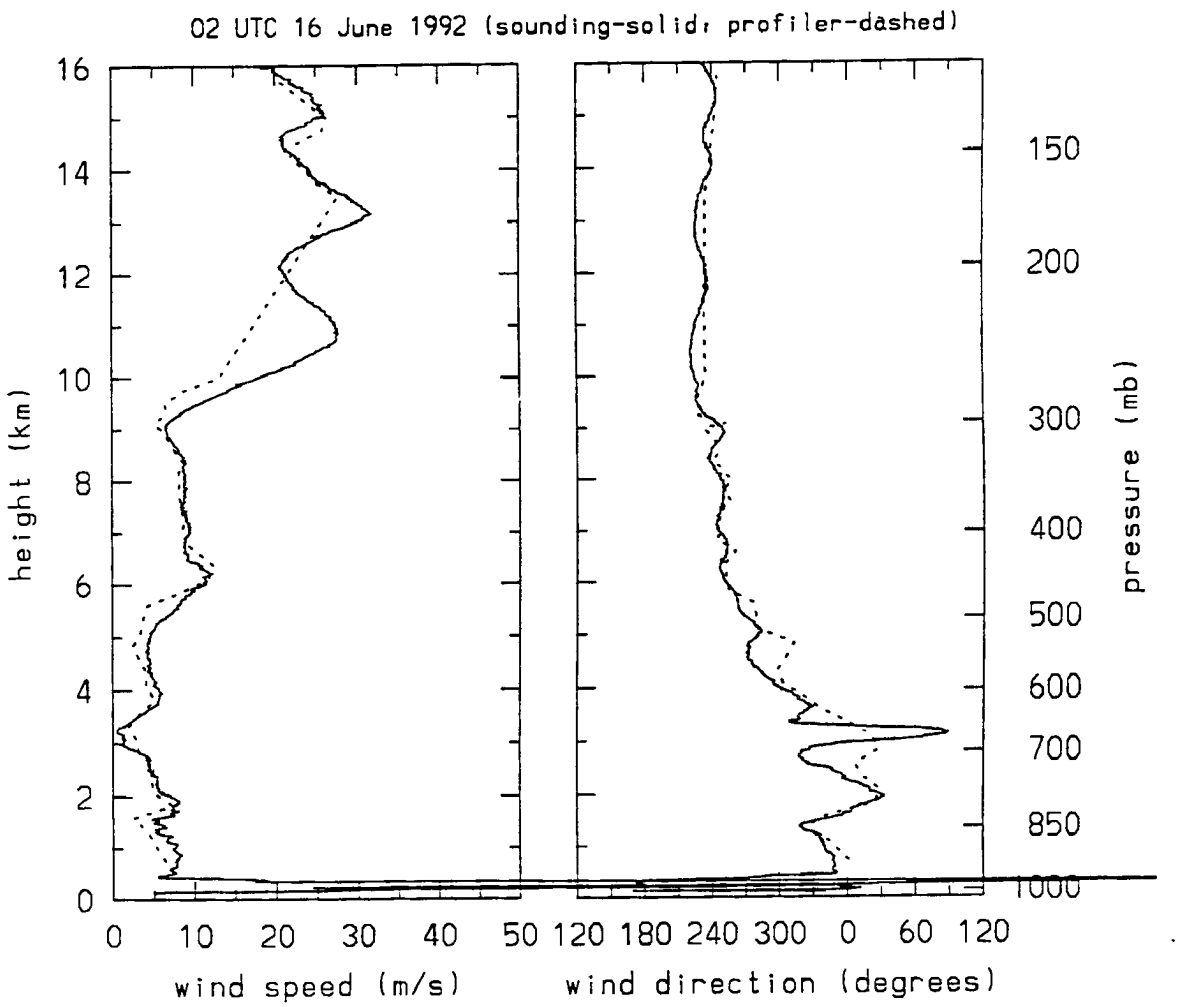

Figure 3.7: Comparison of wind data at 02 UTC, June 16th.

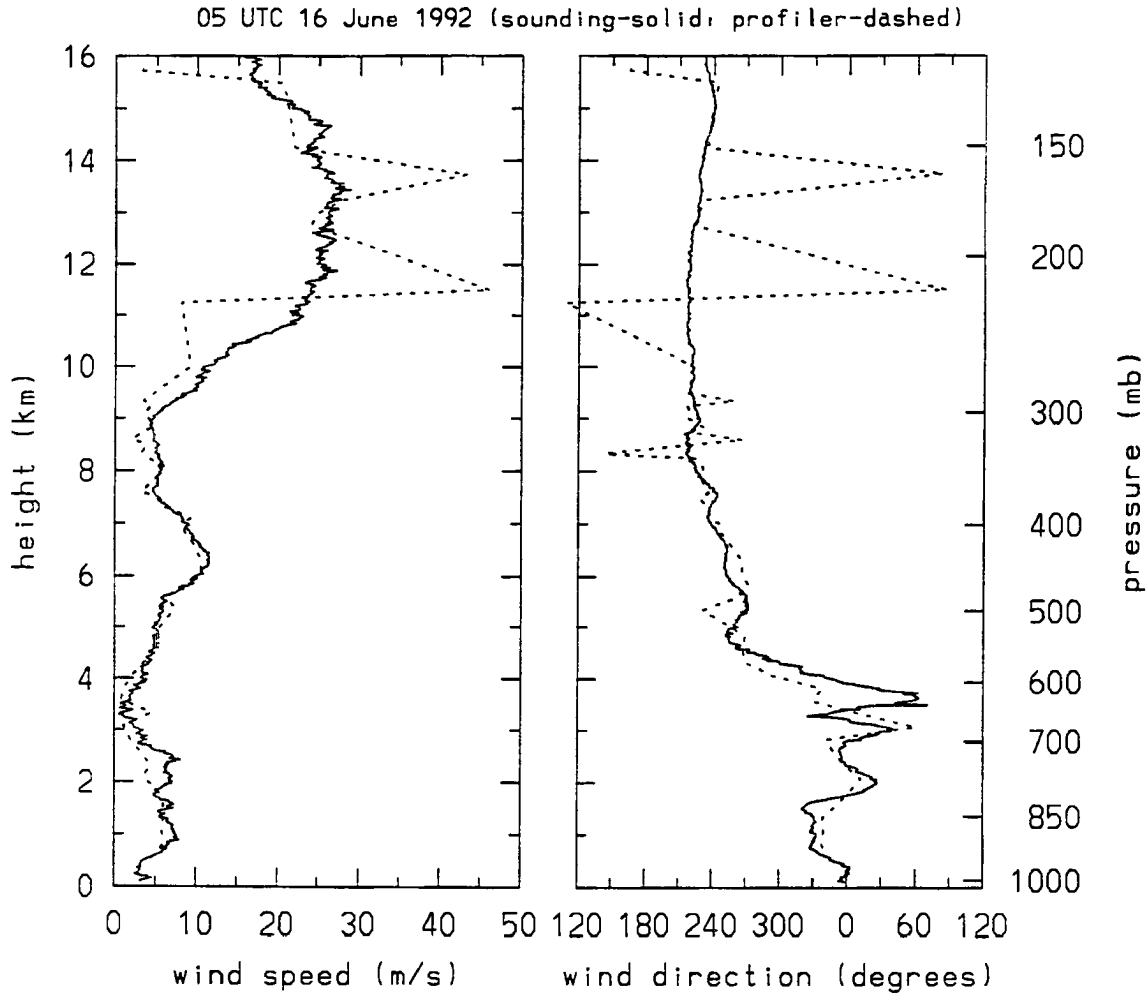

Figure 3.8: Comparison of wind data at 05 UTC, June 16th.

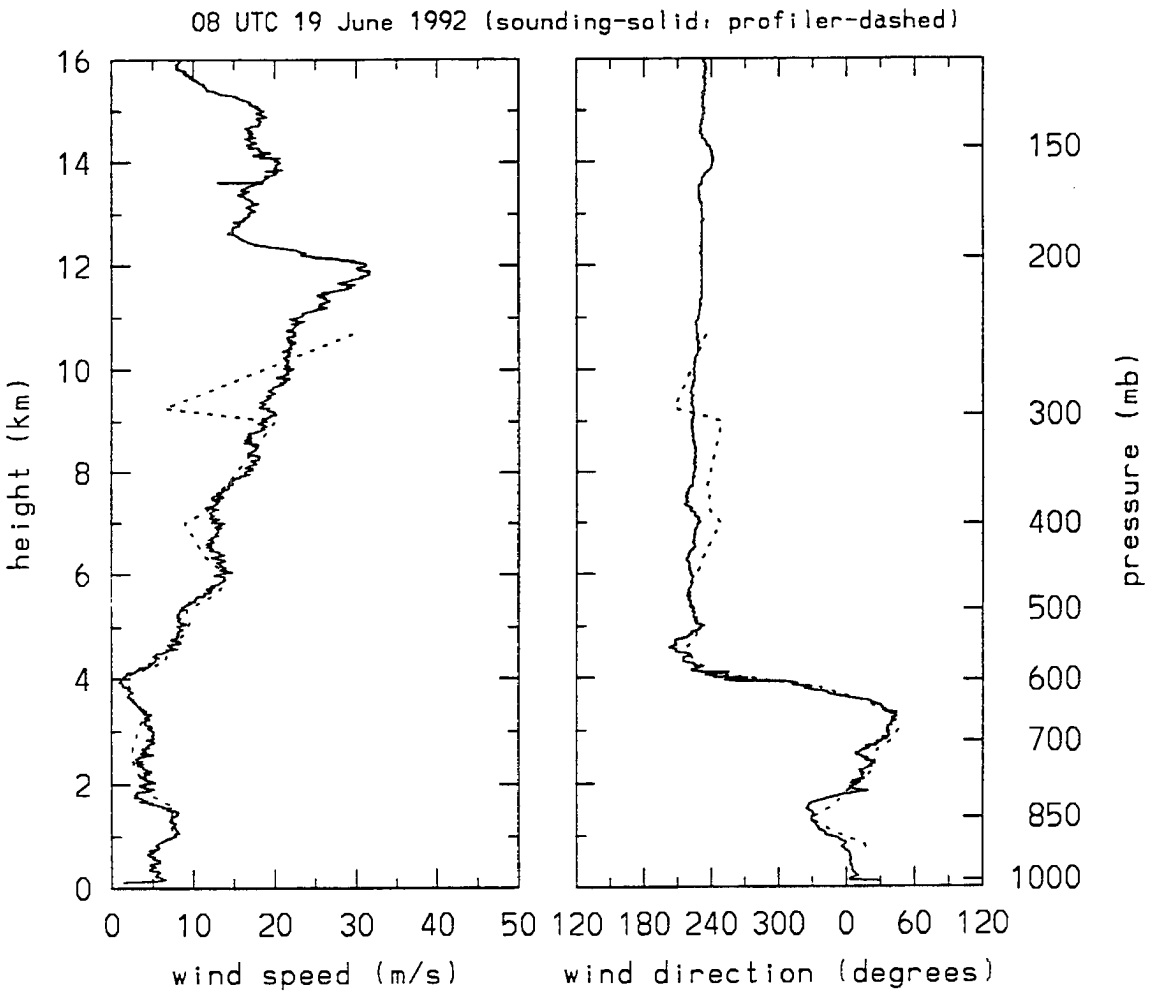

Figure 3.9: Comparison of wind data at 08 UTC, June 19th

The format used in all comparisons of ceilometer, Doppler cloud radar, and radiosonde data is displayed in figure 3.10, where the vertical axis is height above sea level in kilometers, and the horizontal axis is time, marked in UTC hours. Red circles are cloud base heights determined by the ceilometer. Light blue crosses represent cloud base heights as determined by the Doppler cloud radar, and dark blue crosses represent the radar's determination of cloud top. Note that the cloud radar can detect more than one cloud layer at a given moment, while the ceilometer reports only one ceiling. The two black plots at the right of figure 3.10 represent radiosonde thermodynamic data; the right-hand plot is temperature, and the left-hand plot is dew-point. The horizontal axis of plots of radiosonde thermodynamic data is usually temperature, but in this case the radiosonde's horizontal axis is time. This paper is primarily concerned with the difference between the temperature and dew point as opposed to the actual values of temperature and dew point. To properly place the radiosonde data in time, look where the temperature data intersects the 3 km height line—this is the sonde's launch time. Based on an ascent rate of 4 or 5 ms^{-1}, the sonde requires between 10 and 12.5 minutes to reach 3 km. The sounding data should thus be compared to the ceilometer and cloud radar data falling near the sonde's launch time.

Figure 3.10 displays some important characteristics of the entire ASTEX data set. The cloud detected between 3 and 6 UTC just below 1.5 km is stratified, and under such calm conditions the ceilometer and Doppler cloud radar often agree on the height of the cloud base, as they do here in figure 3.10. Notice that the radiosonde detects a saturated layer near the altitude that the ceilometer and radar detected the cloud base but at slightly lower elevation. The radiosonde data also show a pronounced divergence between the temperature and dew point plots above the cloud top, which is a common feature throughout the ASTEX data set. The temperature and dew point plots diverge at least a hundred meters below the cloud radar's determination of cloud top, however. Finally, the isolated data point in both the ceilometer and cloud radar data at 0.8 km elevation 4:15 UTC demonstrates how these two instruments can occasionally detect and agree on the placement of very small features. In addition, the radiosonde data show a layer of nearly saturated air at this lower, almost-cloudy elevation.

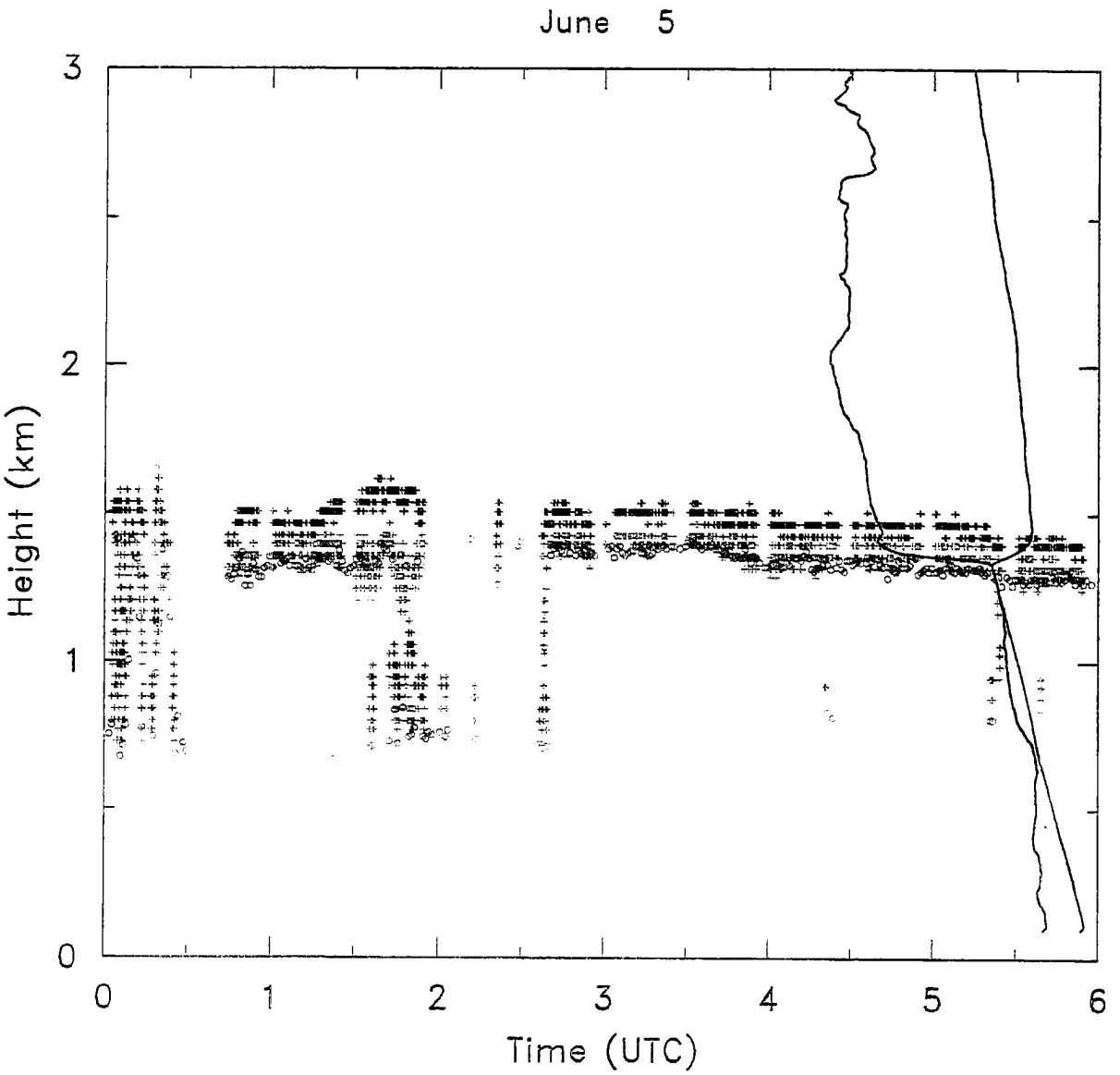

Figure 3.10: Comparison of cloud height data from 0 to 6 UTC , June 5th

Two plots are displayed in figure 3.11. Each plot has been shrunk in the vertical to allow them to be displayed together, but the vertical extent of each plot is still 3 km, and in every other respect the two plots of figure 3.11 are just like figure 3.10. Figure 3.11 covers the first twelve hours of June 14th and presents an interesting time series. Figure 3.11 displays a noisier, less-stratified environment than that found in figure 3.10, and the stratification continues to break down as time approaches 12 UTC. For the first 8 hours the ceilometer and cloud radar agree on the timing of the cloud base's fluctuations in altitude, although they rarely concur on the actual altitude of the cloud base, and when they disagree the ceilometer's value is higher than the cloud radar's. The first three soundings again place cloud top a bit lower than the cloud radar does. After the third sounding the sharply stratified regime exemplified in figure 3.10 decays completely, and no sharp cloud bases or tops are detected by the ceilometer or the cloud radar. The final sounding in figure 3.11 shows that a drying of the boundary layer coincides with the decrease in sharpness of the ceilometer and cloud radar data.

While ceilometer data contain only one cloud base height per minute, the ceilometer is still capable of detecting multiple cloud decks. The ceilometer and Doppler cloud radar each identify two cloud bases in figure 3.12, one at 0.7 km and a second at 1.5 km. When both cloud decks are overhead the ceilometer sometimes detects the lower base and sometimes the higher. When the minute by minute ceilometer data is presented on a scale of six hours, one can see that the ceilometer is in effect detecting two cloud bases simultaneously. The first sounding in figure 3.12 also detects both cloud decks, and the second sounding, much like the fourth sounding in figure 3.11, shows a drying in the boundary layer corresponding to decreases in cloud detection by the ceilometer and radar.

When the ASTEX data are looked at as a whole, neither the ceilometer or the Doppler cloud radar emerges as the finer instrument, consistently seeing details that the other misses. Figures 3.13-15 demonstrate this parity. In figure 3.13 between 12:30 and 15:30 UTC the Doppler cloud radar detects very low clouds under a poorly-defined cloud base at around 0.7 km elevation. The ceilometer occasionally detects the 0.7 km ceiling but never identifies any lower clouds. The first sounding shows the boundary layer to be very moist

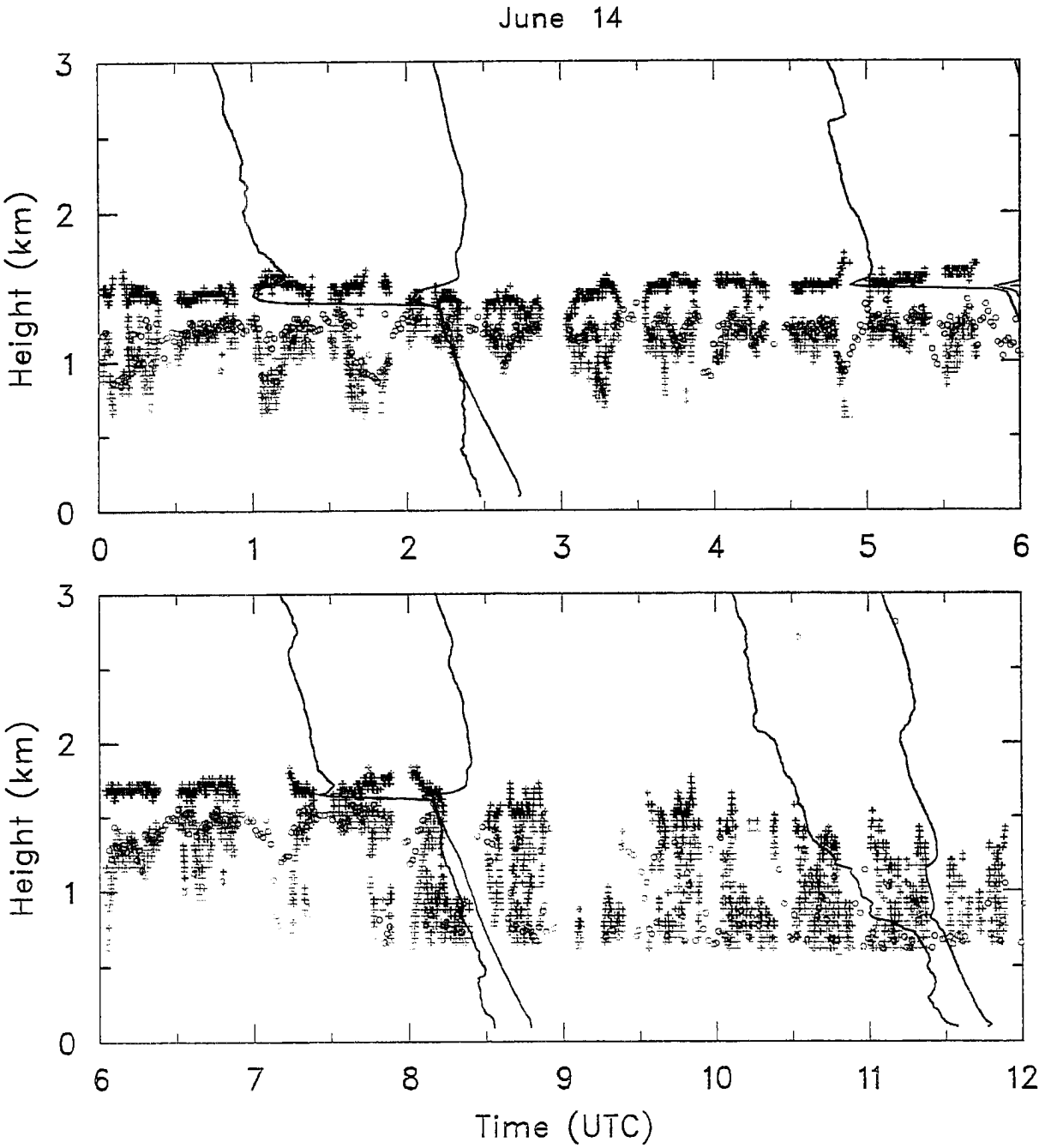

Figure 3.11: Comparison of cloud height data from 0 to 12 UTC, June 14th

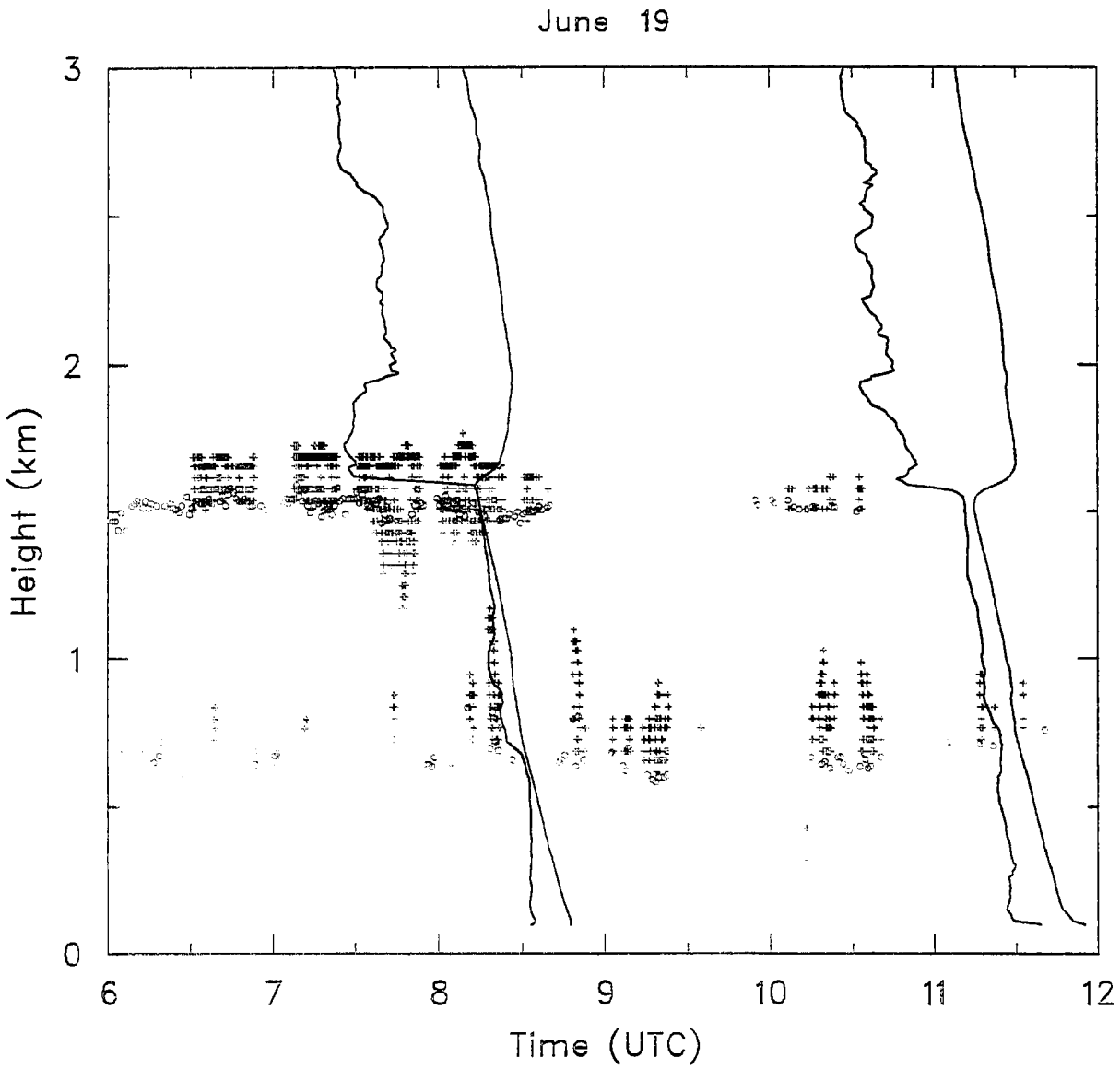

Figure 3.12: Comparison of cloud height data from 6 to 12 UTC, June 19th

but not saturated. Throughout the ASTEX data set the ceilometer and cloud radar have a hard time agreeing on base heights under such moist but non-saturated conditions. In figure 3.14 the ceilometer and cloud radar trade their figure 3.13 roles: the ceilometer now detects a lower cloud base as well as a higher base (although this higher base is less well-defined in the ceilometer data) while the Doppler cloud radar sees only the higher cloud deck. As shown by the two soundings, the boundary layer in figure 3.14 is occasionally saturated, and this is an important difference between figures 3.13 and 3.14. Figure 3.15 displays two six-hour plots in the method of figure 3.11. At 2 UTC the ceilometer and the first sounding detect the cloud at 1.7 km. The cloud radar does not consistently detect this ceiling until 3 UTC (the gaps in radar data after 3 UTC represent times when the radar was occupied with other scan routines). Then in the lower plot the cloud radar has ceased to detect the 1.7 km cloud base by 7 UTC while the ceilometer consistently detects this base past 7:30 UTC. The 8 UTC sounding also places a very thin saturated layer at 1.7 km. Thus in the case of the 1.7 km cloud base, the ceilometer appears to have the sharper eye; the ceilometer detects the forming cloud base before the cloud radar does and continues to detect the dissipating cloud base after the cloud radar can no longer find it. The exact opposite is true for the lower cloud in the same figure, however. From 0 to 8 UTC the Doppler cloud radar occasionally detects a cloud between 0.4 and 1.0 km. After 8 UTC the radar's detection of this lower cloud becomes more regular, and by 11 UTC the ceilometer is also detecting it. The figure's final sounding reveals significant moistening between 0.6 and 1.0 km by 11 UTC as the lower cloud becomes more substantial.

3.3 Data Categorizations

All wind and cloud deck figures from the entire ASTEX data set were subjectively categorized. The wind data were categorized based on average wind direction below 850 mb, and, while the Azores High kept Porto Santo under a predominantly northerly flow, three distinct flow regimes were found, one of which included southerly winds at the surface. Three traits in the cloud deck data were also categorized: the number of cloud decks, the degree of stratification of these decks, and the extent of saturation found

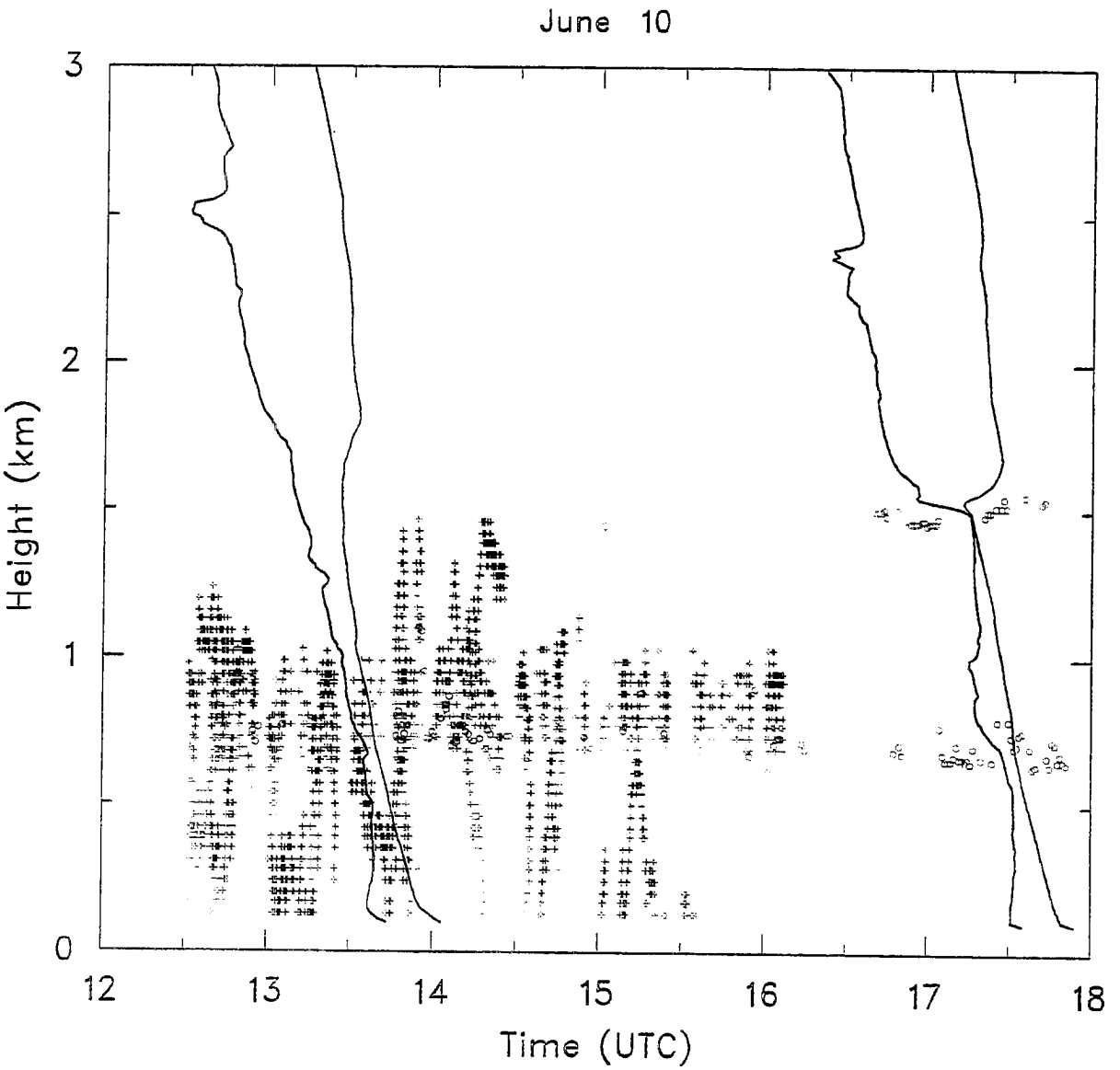

Figure 3.13: Comparison of cloud height data from 12 to 18 UTC, June 10th

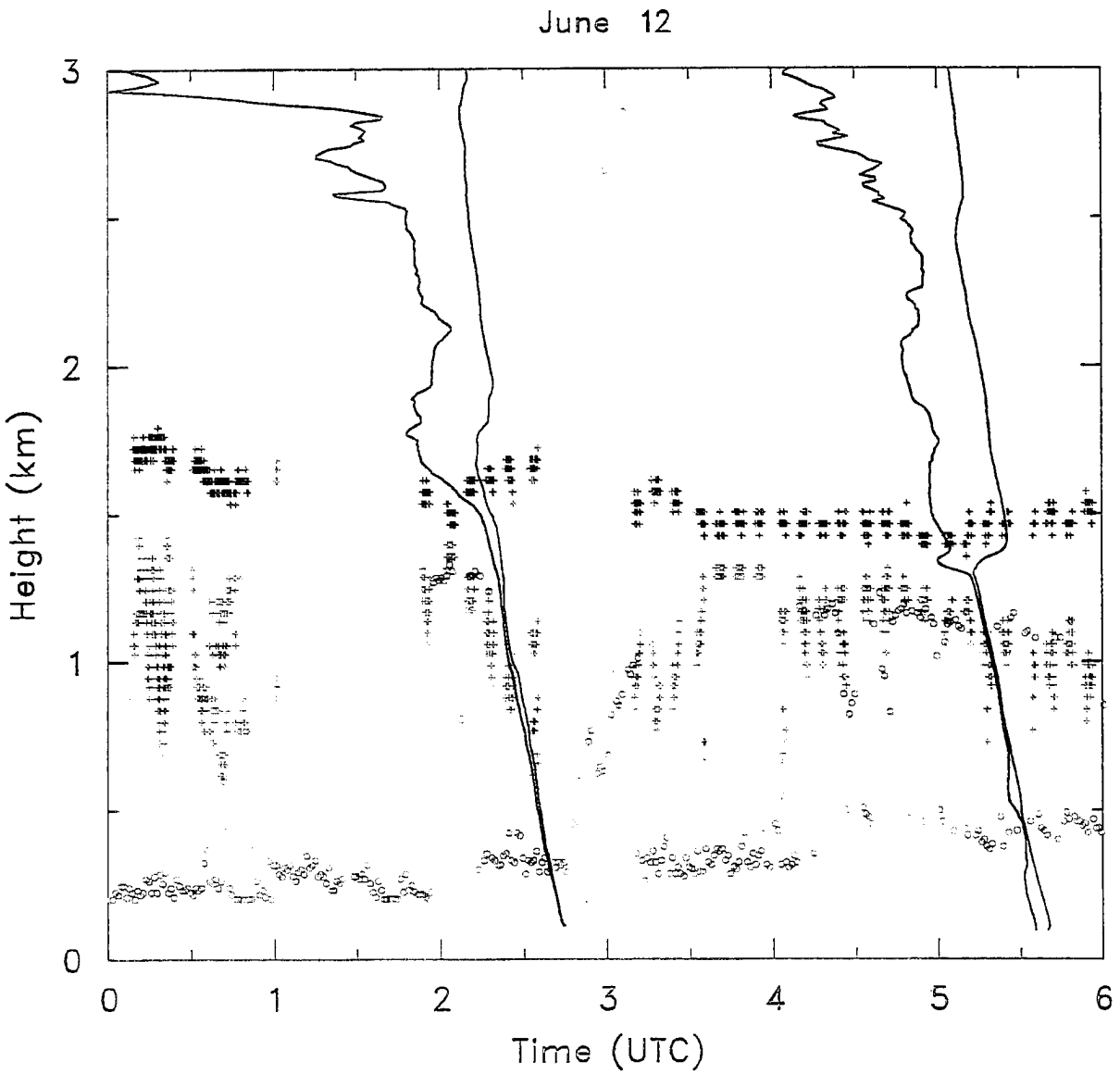

Figure 3.14: Comparison of cloud heighht data from 0 to 6 UTC, June 12th

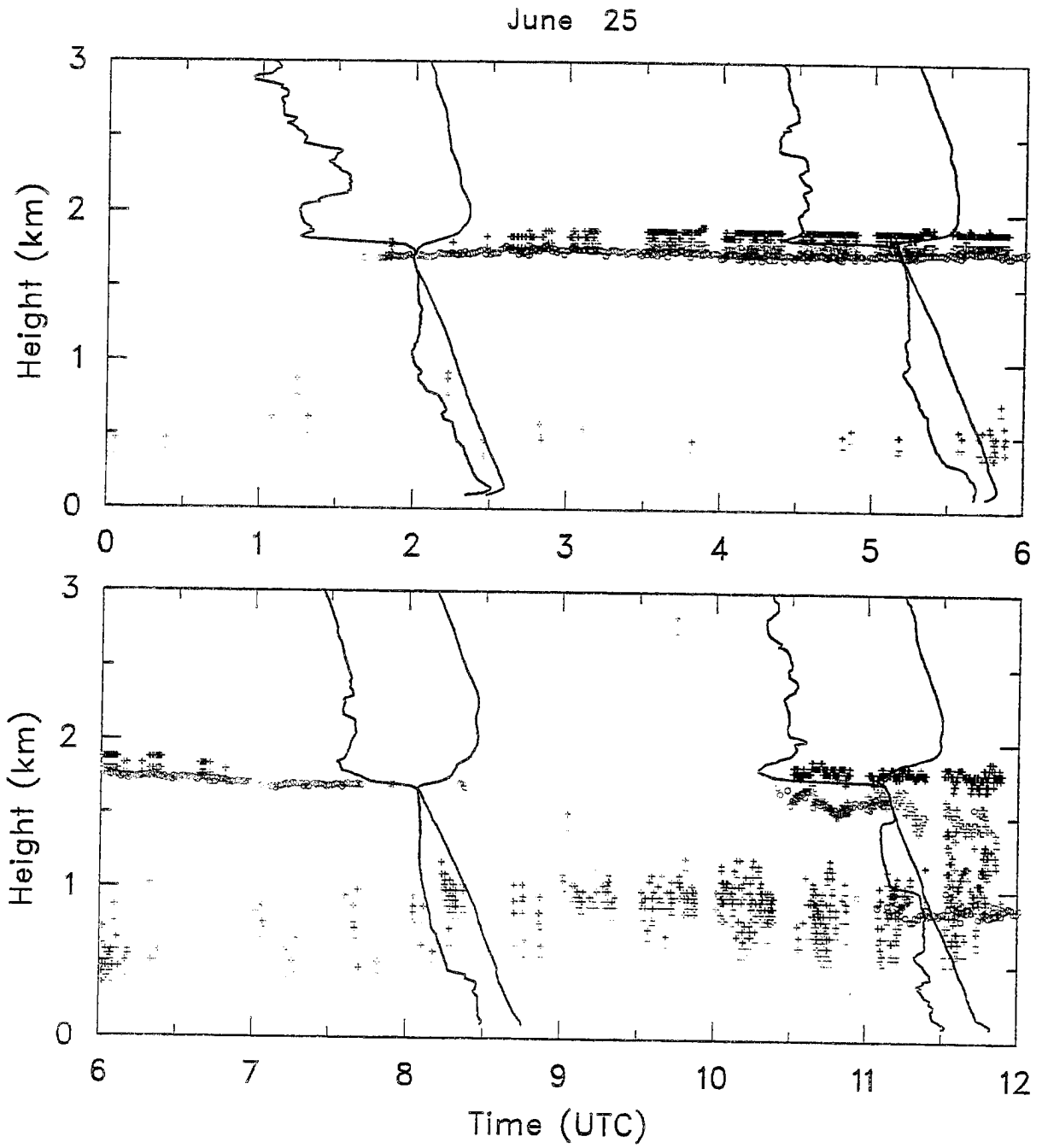

Figure 3.15: Comparison of cloud height data from 0 to 12 UTC, June 25th

in the radiosonde thermodynamic profiles. Almost half the ASTEX data showed two distinct cloud decks. Of all cloud decks slightly more than half had a moderate degree of stratification, and the most common type of sounding was one classified as dry, having no saturated layers, although such dry cases accounted for only a third of the soundings.

The wind direction data below 850 mb were divided into three time periods, and during each period a different flow regime dominated. The first period was the longest and covered data from the beginning of the experiment to 17 UTC, June 24th. Winds below 850 mb blew primarily from the north-northwest during this first period. Average values of wind direction below 850 mb were used, although in this first period not much averaging was required since there was little directional shear with height. Figure 3.1 provides a good representation of the wind direction below 850 mb during this period. Notice that the lowest level in the wind profiler's data is about 900 mb in figure 3.1. As mentioned in Chapter Two, wind profilers have a minimum range below which they are blind. All ASTEX wind profiler data begin at 900 mb, as seen in figure 3.1, and thus radiosonde data are more useful for wind categorization below 850 mb. The second period covered sondes launched between 20 UTC, June 24th through 08 UTC, June 27th. This period saw a substantial increase in directional shear below 850 mb. In figure 3.16 winds are still out of the north at the surface, but on the way up to 850 mb the winds turn to blow from 150° and then turn back to blow from the north before becoming westerly. During this second period the surface winds still blow predominantly out of the north, despite the increasing low-level directional shear. The third period, from 11 UTC, June 27th through the end of the experiment, was characterized by southerly surface winds while at 850 mb winds were generally westerly. Figure 3.17 is an example of the winds in this final period.

Cloud deck traits categorized were the number of cloud decks, the degree of stratification within these decks, and the extent to which radiosonde profiles were saturated. Each six-hour cloud data segment was assigned one of four values for its number of cloud decks. The values included no clouds, a low cloud deck (typically with bases at or below 1 km), a high cloud deck (typically with bases at or above 1.5 km), and both low and high

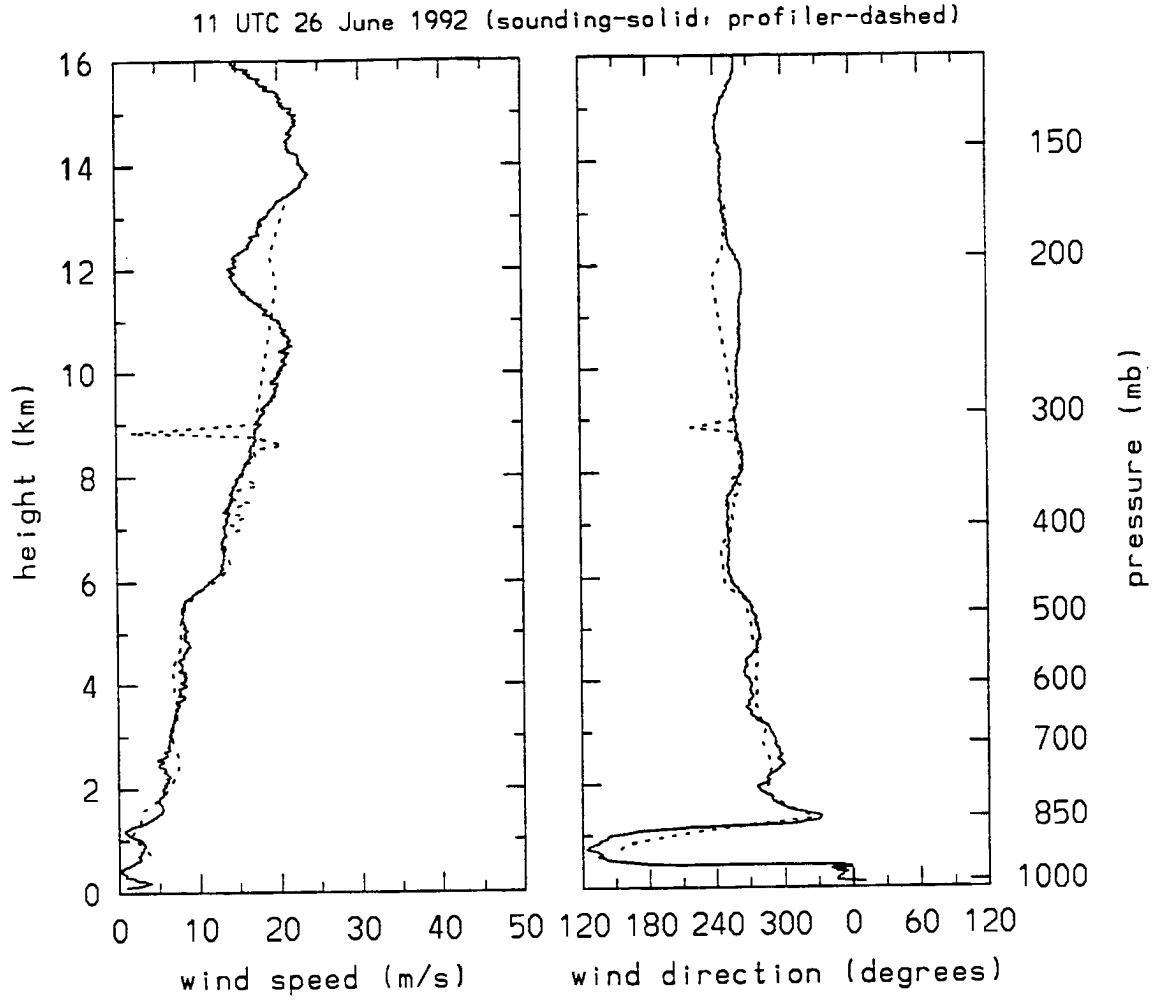

Figure 3.16: Wind data from 11 UTC, June 26th.

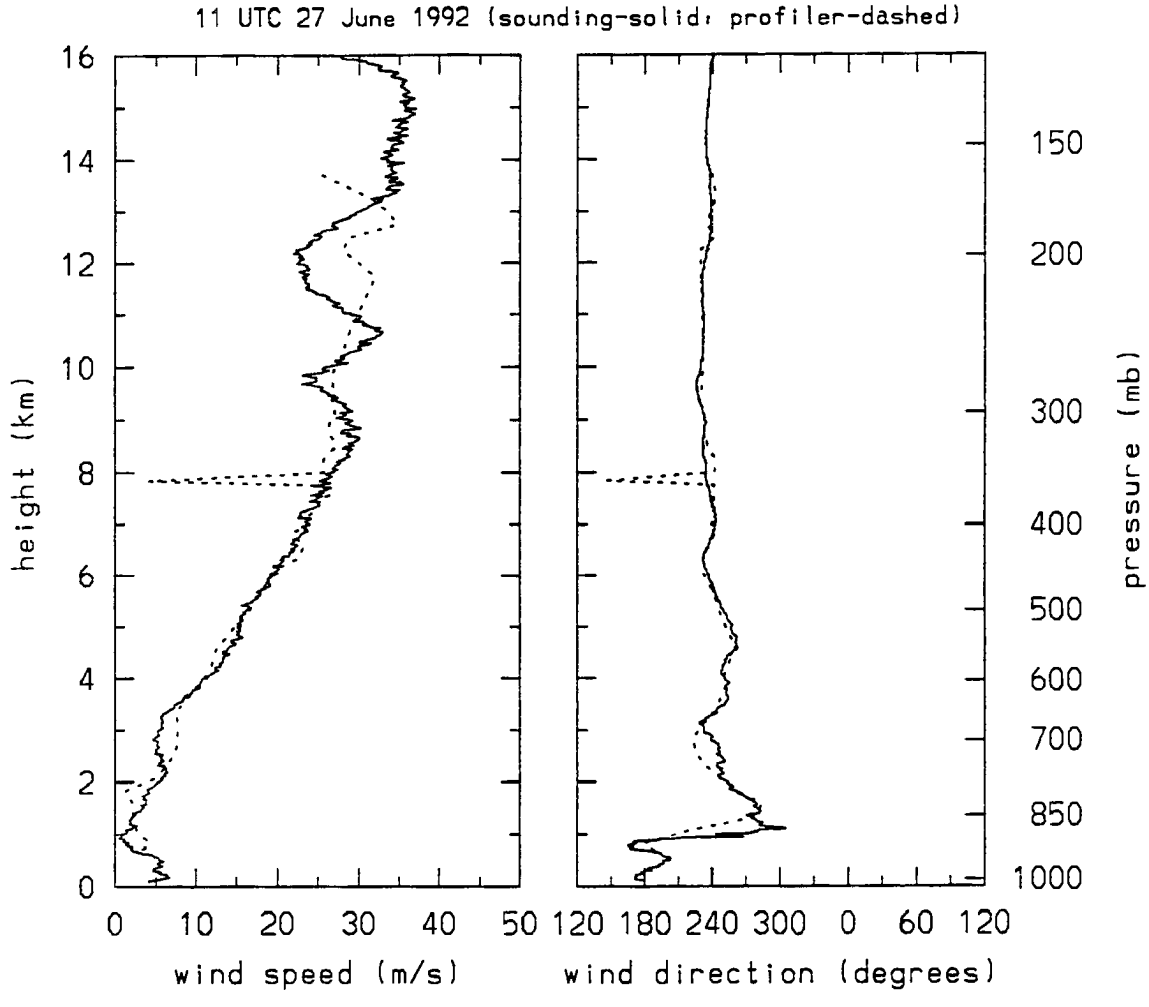

Figure 3.17: Wind data from 11 UTC, June 27th.

cloud decks. Only one value was assigned to each six-hour segment, and often different cloud decks passed in and out of existence during the six hours. Thus an average, representative value was chosen, and such a value might not accurately describe the entire six-hour segment. Figure 3.10 can serve as an example of how various cloud deck traits are categorized. Figure 3.10 has been classified as having both low and high clouds. There is obviously a high cloud in this figure, but the low cloud is more tenuous. If it weren't for the somewhat-consistent nature of the lower deck between 0 and 3 UTC, this segment would have been categorized as high cloud only. The following table lists frequencies of the various cloud deck classifications found in the entire ASTEX data set.

Number of cloud decks	
decks	**% of data set**
none	5.5
low	33.6
high	11.8
low and high	49.1

Each cloud deck, at whatever altitude, was assigned one of three degrees of stratification: stratified, less stratified, or disorderly. The high cloud deck in figure 3.10 is classified as stratified, while the lower deck is classified as less stratified. The table below lists the prevalence of each degree of stratification compiled from the classification of each cloud deck.

Stratification of decks	
stratification	**% of cloud decks**
stratified	22.8
less stratified	54.4
disorderly	22.8

Notice that a majority of clouds were classified as less stratified, the middle of the road value. This middle-heavy distribution is most likely the result of assigning consensus values to the six hour segments; extreme, short-lived characteristics often canceled each other, leaving many cloud decks described as less stratified.

Radiosonde thermodynamic profiles were classified with regard to layers of saturation. The sondes frequently detected saturated air in the vicinity of cloud decks, and the possible

saturation profiles reflect the distribution of the clouds. The possible profiles are: low, in which the profile is saturated only in the region of the low cloud deck; high, in which the profile is saturated only in the region of the high cloud deck (figure 3.10 has a profile with a high saturated region); low and high, in which the low and high deck regions are both saturated but the area between them is dry (figure 3.10 is almost in this category, but the low cloud region is not quite saturated); throughout, in which the low and high deck regions are both saturated, as well as the area between them; and dry, where there is no saturation. The following table outlines the saturation distribution.

Saturation layers	
saturation layers	**% of soundings**
low only	18.5
high only	23.4
low and high	16.8
throughout	7.1
dry	34.2

Data containing the number of cloud decks were recorded along with the degrees of stratification of these decks. As in the case when all cloud decks were viewed together, the majority of both the low and high cloud decks are classified as less stratified:

Low cloud stratification	
cloud and stratification	**% of cloud decks**
low stratified	19.8
low less stratified	53.8
low disorderly	26.4

High cloud stratification	
cloud and stratification	**% of cloud decks**
high stratified	26.9
high less stratified	55.2
high disorderly	17.9

The four tables below list saturation distributions, given a certain cloud deck configuration.

Low and high cloud decks and saturation	
cloud and saturation	**% of sondes**
low and high clouds, sounding sataurated low	10.4
low and high clouds, sounding saturated high	25.0
low and high clouds, sounding saturated low and high	27.1
low and high clouds, sounding saturated throughout	11.5
low and high clouds, sounding dry	26.0

Low cloud deck and saturation	
cloud and saturation	**% of sondes**
low cloud, sounding sataurated low	38.7
low cloud, sounding saturated high	6.5
low cloud, sounding saturated low and high	6.5
low cloud, sounding saturated throughout	3.2
low cloud, sounding dry	45.2

High cloud deck and saturation	
cloud and saturation	**% of sondes**
high cloud, sounding saturated low	7.7
high cloud, sounding saturated high	69.2
high cloud, sounding saturated low and high	3.8
high cloud, sounding saturated throughout	3.8
high cloud, sounding dry	15.4

No cloud deck and saturation	
cloud and saturation	**% of sondes**
no cloud, sounding saturated low	9.1
no cloud, sounding saturated high	18.2
no cloud, sounding saturated low and high	0.0
no cloud, sounding saturated throughout	0.0
no cloud, sounding dry	72.7

Notice the strong showing of the dry soundings in the four tables above. As could be expected, dry profiles accounted for a majority of the soundings taken under skies classified as having no clouds. But under the other three cloud classifications, dry soundings were at least the second-largest sounding group, and under low cloud conditions dry soundings accounted for a larger percentage of total soundings than did soundings saturated at the low cloud's altitude. A possible factor contributing to the prevalence of dry soundings in the above tables is the chosen definition of a saturated level: to be called saturated,

the temperature and dew point plots must touch. Throughout the ASTEX data set there are many cases in which a sounding was almost saturated in the vicinity of a cloud but was still classified as dry, as exemplified by the thermodynamic profile at around 1.4 km in figure 3.10. Another factor to consider when looking at the saturation distributions is that the sondes take ten to twelve minutes to ascend above 3 km, while the sonde's data are being compared to six hour's worth of ceilometer and cloud radar data. Sondes may thus be launched at unrepresentative times.

Two points must be remembered when viewing all of the tables. First, in all the categorizations presented in this section, every cloud deck and sounding was categorized. If a cloud or sounding didn't fit nicely into one of the common classifications, it was forced into the closest group; no room was made for a category called "rebel." Second, as in the case with the categorization of wind direction data, these classifications are very subjective, and should not be interpreted as a rigorous statistical analysis.

Chapter 4

SUMMARY AND CONCLUSIONS

In this paper four instruments, the AIR Intellisonde Rawin System, the Colorado State University wind profiling radar, the Wave Propagation Laboratory's 8.7 mm wavelength Doppler cloud radar, and the Belfort laser ceilometer, were described, as were the data gathered by these instruments at Porto Santo Island during ASTEX, June, 1992.

Several inherent inaccuracies in the radiosonde system's thermodynamic and wind measurements were discussed. The effect of instrument time lag, or errors caused by the sonde's sensors requiring an amount of time to notice a temperature change, was described. Such lag effects in temperature and relative humidity are not always negligible, especially in strong inversions, but no attempt was made to correct these errors in the ASTEX radiosonde data. The tendency for a balloon to require time to match its horizontal motion with that of the surrounding air while ascending through sheared layers, known as inertial lag, was found to have a negligible effect on the wind data. The balloons used during ASTEX may have experienced self-induced oscillations as they ascended, but the AIR system software was designed to filter out errors caused by such oscillations.

The cleaning of the radiosonde thermodynamic data was discussed, as was the derivation of dew point temperature T_d from temperature T and relative humidity U. The radiosonde wind data were filtered by the AIR system software. Colorado State University's wind profiling radar and its data were described. The wind profiler data were averaged over one hour and cleaned, and in so doing many range gates were deleted, most commonly because of poor vertical velocity calculations. The wind profiler lost accuracy at higher altitudes, and here the cleaning algorithm left some hourly-averaged data files with skeletal profiles. In a comparison with other ceilometers, the Belfort laser ceilometer was

found to be somewhat less sensitive to clouds than other ceilometers. According to the same comparison, however, the Belfort model consistently agreed with the other ceilometers regarding ceiling height once it had detected a cloud base. The ceilometer data were cleaned using the Klett algorithm and organized into minute by minute values of cloud base height.

Once the data were cleaned, two comparisons were made: first radiosonde and wind profiler winds were compared, and next ceilometer, Doppler cloud radar, and radiosonde cloud base heights and cloud top heights were compared.

The radiosonde and wind profiler winds were split into plots of wind speed and wind direction. Inaccurate wind profiler data points occasionally survived cleaning and manifested themselves as spikes in both the wind speed and wind direction plots. Overall the two instruments' data agreed very well in both speed and direction, although the wind profiler's data often became sparse at higher elevations.

Under stably stratified conditions the ceilometer and Doppler cloud radar determinations of cloud base height showed good agreement, but the two instruments agreed less under more neutral conditions. Unlike the cloud radar, the ceilometer was only capable of detecting one cloud base at a time. Despite this apparent limitation, the ceilometer often detected the bases of two clouds by detecting one cloud base one minute and another cloud base the next minute, and so on. When its one-minute data were viewed on a time scale of hours, the ceilometer in effect found two cloud decks simultaneously. In comparison to the ceilometer and cloud radar, the radiosonde slightly underestimated the height of cloud decks, both base and top, under stratified conditions as well as more chaotic conditions. Neither the ceilometer nor the cloud radar emerged as superior in detecting very subtle features under conditions which the radiosonde determined were moist but still sub-saturated; the ceilometer occasionally detected features that the radar missed, and occasionally these rolls were reversed.

After the data comparisons had been made, several characteristics of the data were categorized. Wind direction below 850 mb fell into three distinct regimes, with the third regime providing an unusual southerly flow at the surface. Cloud data were categorized

according to number of cloud decks, degree of stratification of these cloud decks, and distribution of saturation within radiosonde thermodynamic data. The simultaneous appearance of a low and high cloud deck was the most common cloud distribution, and these clouds most likely were characterized by a moderate degree of stratification. Completely dry soundings occurred more frequently than any other saturation profile.

Overall, the four instruments agreed quite well during ASTEX, with the exception of one systematic discrepancy: the radiosonde's placement of saturated layers was generally slightly lower than the ceilometer and cloud radar's determination of cloud base and the cloud radar's determination of cloud top.

REFERENCES

Bolton, D., 1980: The Computation of Equivalent Potential Temperature. *Mon. Wea. Rev.*, **108**, 1046-1053.

Clem, L.H., D. Colson, and L.P. Harrison, 1954: Corrections of Upper-Level Wind Computations for Effect of Earth's Curvature. *Bull. Amer. Meteor. Soc.*,, **35**, 357–362.

Cox, S., C. Cornwall, W. Cotton, J. Davis, J. Kleist, T. McKee, Q. Shao, D. Randall, W. Schubert, D. Wood, S. Frisch, M. Hardesty, R. Kropfli, J. Snider, and P. Anikin, 1993: CSU/NOAA-WPL FIRE II–ASTEX Field Experiment Description of Field Deployment Phase. Colorado State University, Department of Atmospheric Science, Report No. 523, 122 pp.

FIRE Project Office, 1992: ASTEX Operations Plan. Available from David S. McDougal, FIRE Project Manager, Mail Stop 483, NASA Langley Research Center, Hampton, VA 23665-5225.

Hamming, R.W., 1983: *Digital Filters*, Second Edition. Prentice-Hall, Englewood Cliffs, New Jersey, 257 pp.

Huschke, R.E., 1959: *Glossary of Meteorology*, American Meteorological Society, Boston, Massachusetts, 638 pp.

Jones, R.F., 1968: Use of Ground-Based Radar in Meteorology (Excluding Upper-Wind Measurements). World Meteorological Organization, Technical Note No. 78, 104 pp.

Klett, J.D., 1981: Stable Analytical Inversion Solution for Processing Lidar Returns. *Applied Optics*, **20**, 211-220.

—, 1986: Extinction Boundary Value Algorithms for Lidar Inversion. *Applied Optics*, **25**, 2462–2464.

—, 1991: Lidar Inversion Algorithms for Belfort Instrument Co., Report and Software Documentation. Belfort Instrument Co.

Levy, R., D. Randall, and W.H. Schubert, 1993: An Overview of the ASTEX Data Collected at Porto Santo. Colorado State University, Department of Atnmospheric Science, Report No. 539, 58 pp.

Martner, B.E. and R.A. Kropfli, 1993: Observations of Multi-layered Clouds using K_α-Band Radar. FIRE Cirrus Science Results, 1993. NASA Conference Publication 3238, 75–82.

McVehil, G.E., R.J. Pilié, and G.A. Zigrossi, 1965: Some Measurements of Balloon Motions with Doppler Radar. *J. Appl. Meteor.*, **4**, 146–148.

Murrow, H.N. and R.M. Henry, 1965: Self-Induced Balloon Motions. *J. Appl. Meteor.*, **4**, 131–138.

Ouldridge, M., D.W. Jones, and D.J. Painting, 1989: The WMO International Ceilometer Intercomparison, Beaufort Park 1986. *Met. Magazine*, **118**, 242–246.

Perkins, D.T., 1952: The Response of Balloons to the Wind. *Bull. Amer. Meteor. Soc.*, **33**, 135-139.

Peterson, V.L., 1988: Wind Profiling–The History, Principles, and Applications of Clear-air Doppler Radar. Tycho Technology, Inc.

Schubert, W.H., S.K. Cox, T.B. McKee, D.A. Randall, P.E. Ciesielski, J.D. Kleist, and E.L. Stevens 1992: Analysis of Sounding Data from Porto Santo Island During ASTEX. Colorado State University, Department of Atmospheric Science, Report No. 512, 96 pp.

Scoggins, J.R., 1965: Spherical Balloon Wind Sensor Behavior. *J. Appl. Meteor.*, **4**, 139–145.

Wexler, A., 1976: Vapor Pressure Formulation for Water in Range 0 to 100°C. A revision. *J. Res. Nat. Bur. Stand.*, **80A**, 775-785.